DARPA CMUVT Contract FA2386-10-1-4152 Final Report Phase II

Performers: Georgia Institute of Technology, Arizona State University
Submitted by Russell D. Dupuis, PI
Center for Compound Semiconductors
School of ECE, Georgia Institute of Technology,
777 Atlantic Drive NW, Atlanta, GA 30332-0250

Performers:
Zachary Lochner,[1] Tsung-Ting Kao,[1] Yuh-Shiuan Liu,[1] Xiao-Hang Li,[1] Md. Mahbub Satter,[1] Shyh-Chiang Shen (Co-PI),[1] P. Douglas Yoder (Co-PI),[1] Jae-Hyun Ryou,[1,a] Theeradetch Detchprohm,[1] and Russell D. Dupuis (PI),[1] Yong Wei,[2] Hongen Xie,[2] Alec Fischer,[2] and Fernando A. Ponce (Co-PI)[2]

[1] Center for Compound Semiconductors and School of Electrical and Computer Engineering, Georgia Institute of Technology, 777 Atlantic Dr. NW, Atlanta, Georgia 30332-0250, USA
[2] Department of Physics, Arizona State University, Tempe, AZ 85287-1504, U.S.A.
[a)] Now at Dept. of Mech. Eng., Univ. Houston, Houston TX

The overall goals of this program are to develop III-N deep-UV injection lasers operating at $\lambda<250$nm at 300K with CW output power greater than 5mW. The Georgia Tech program is divided into four primary tasks: (1) III-N Materials Growth and Evaluation; (2) Detailed III-N Materials Characterization; (3) III-N UV laser design and simulation; and (4) III-N UV laser processing, testing, and characterization. The recent efforts by the Georgia Tech/ASU team are summarized below. This report will focus on the recent work in the past six months of the program.

Summary of Overall Program Major Accomplishments:

1. We have developed MOCVD growth technologies for III-N deep-UV lasers on two different growth systems: the "standard" Thomas-Swan 6x2 Close-Coupled Showerhead MOCVD reactor using AlGaN-AlN growth conditions at ~1150C, and one new high-temperature AIXTRON 3x2 Close-Coupled Showerhead MOCVD system operating at up to ~1300C, (which was purchased partially with funds from this program), to allow us to explore "higher temperature" growth regimes.
2. We have exploited advanced high-resolution materials growth technologies, e.g., high-angle annular dark-field (HAADF) imaging, Rutherford Back Scattering, high-resolution TEM, and variable-temperature cathodoluminescence, to characterize the III-N wide-bandgap materials.
3. We have developed the most complete and advanced III-N device simulation tool and have utilized it to optimize the optical and electrical performance of deep-UV laser diodes at ~250nm.
4. We have developed and exercised the required III-N UV laser device processing, wafer thinning, facet cleaving, facet coating, and optical characterization techniques and exploited these processes to demonstrate optically pumped pulsed UV lasers at $\lambda<250$nm with thresholds as low as ~297 kW/cm^2 for lasers at $\lambda=245.3$ nm without facet coatings.
5. Additional studies of optically pumped lasers with one facet coated has shown 300K lasing at

Report Documentation Page

Form Approved
OMB No. 0704-0188

1. REPORT DATE	2. REPORT TYPE	3. DATES COVERED
15 NOV 2013	**Final**	**01-09-2010 to 01-08-2013**

4. TITLE AND SUBTITLE
ADVANCED MIDDLE-UV COHERENT OPTICAL SOURCES

5a. CONTRACT NUMBER
FA23861014152

5b. GRANT NUMBER

5c. PROGRAM ELEMENT NUMBER

6. AUTHOR(S)
Russell Dupuis

5d. PROJECT NUMBER

5e. TASK NUMBER

5f. WORK UNIT NUMBER

7. PERFORMING ORGANIZATION NAME(S) AND ADDRESS(ES)
Georgia Institute of Technology,777 Atlantic Drive ,NW,Atlanta,AT,30332-0250

8. PERFORMING ORGANIZATION REPORT NUMBER
N/A

9. SPONSORING/MONITORING AGENCY NAME(S) AND ADDRESS(ES)
AOARD, UNIT 45002, APO, AP, 96338-5002

10. SPONSOR/MONITOR'S ACRONYM(S)
AOARD

11. SPONSOR/MONITOR'S REPORT NUMBER(S)
AOARD-104152

12. DISTRIBUTION/AVAILABILITY STATEMENT
Approved for public release; distribution unlimited

13. SUPPLEMENTARY NOTES

14. ABSTRACT
We have developed MOCVD growth technologies for III-N deep-UV lasers on two different growth systems: the ?standard? Thomas-Swan 6x2 Close-Coupled Showerhead MOCVD reactor using AlGaN-AlN growth conditions at ~1150C, and one new high-temperature AIXTRON 3x2 Close-Coupled Showerhead MOCVD system operating at up to ~1300C, to allow us to explore ?higher temperature? growth regimes. We have exploited advanced high-resolution materials growth technologies, to characterize the III-N wide-bandgap materials. We have developed the most complete and advanced III-N device simulation tool and have utilized it to optimize the optical and electrical performance of deep-UV laser diodes at ~250nm. We have developed and exercised the required III-N UV laser device processing, wafer thinning, facet cleaving, facet coating, and optical characterization techniques and exploited these processes to demonstrate optically pumped pulsed UV lasers at <250nm with thresholds as low as ~297 kW/cm2 for lasers at 245.3 nm without facet coatings. Additional studies of optically pumped lasers with one facet coated have shown 300K lasing at 249nm and threshold of 230 kW/cm2. Optically pumped lasers at 249 nm have also been demonstrated with thresholds as low as 180kW/cm2 for laser bars with facet coatings on both facets. Developed n-type and p-type doping for AlGaN-based cladding layers for deep-UV lasers. The testing of our first complete UV laser p-n junction diode structures grown on AlN substrates was completed and the I-V characteristics and EL spectra were measured. However, no laser operation was observed at 300K under pulsed conditions.

15. SUBJECT TERMS
UV LEDs, Laser

16. SECURITY CLASSIFICATION OF:			17. LIMITATION OF ABSTRACT	18. NUMBER OF PAGES	19a. NAME OF RESPONSIBLE PERSON
a. REPORT **unclassified**	b. ABSTRACT **unclassified**	c. THIS PAGE **unclassified**	**Same as Report (SAR)**	**55**	

Standard Form 298 (Rev. 8-98)
Prescribed by ANSI Std Z39-18

λ=249 and threshold of 230 kW/cm^2

6. Optically pumped lasers at λ = 249 nm have also been demonstrated with thresholds as low as 180kW/cm^2 for laser bars with facet coatings on both facets.
7. Developed *n*-type and *p*-type doping for AlGaN-based cladding layers for deep-UV lasers.
8. The testing of our first complete UV laser *p-n* junction diode structures grown on AlN substrates was completed and the *I-V* characteristics and EL spectra were measured. However, no laser operation was observed at 300K under pulsed conditions.

TASK 1: III-N Materials Growth and Evaluation

Zachary Lochner, Xiaohang Li, Yuh-Shiuan Liu, Jae-Hyun Ryou, Theeradetch Detchprohm, and Russell D. Dupuis, Georgia Tech-Atlanta

1.1 Development of AlGaN UV lasers by MOCVD in Thomas Swan CCS System

In the recent six-month period, the focus of the MOCVD growth studies in the Thomas Swan MOCVD system shifted to electrical performance of wide-bandgap AlGaN ternary alloys. Various silicon-doped (*n*-type) and magnesium-doped (*p*-type) AlGaN alloys with different aluminum molar fraction were explored. To ensure measurement accuracy, three different electrical characterization methods were employed, including Lehighton sheet resistance mapping, Hall measurement, and circular transmission line measurement (CTLM). A 250 nm thick of doped AlGaN layer was grown on top of an un-doped graded buffer layer for electrical characterizations. The graded buffer was used to alleviate the polarization charge between AlN and AlGaN interface.

Table 1 summarized the optimized electrical characteristics for various *n*-type AlGaN, including free electron concentration (n), electron mobility (μ), and bulk resistivity (ρ). Vanadium-based metal alloy (V/Al/Ti/Au) was employed to form Ohmic contact for CTLM and Hall measurement. A significant increase in the bulk resistivity starting from aluminum molar fraction above 60% was observed. In addition, once the aluminum molar fraction reaches ~80%, material becomes highly resistive. Similar observation in bulk n-type AlGaN resistivity was reported by Katsuno, et al.[1] and Nakarmi, et al.[2]

Table 1. Summary of electrical properties from *n*-type AlGaN.

Sample Description	n (cm^{-3})	μ (cm^2/V·s)	ρ (Ω·cm)
n-$Al_{0.8}Ga_{0.2}N$	2.7e+17	4.608	5
n-$Al_{0.73}Ga_{0.27}N$	7.1e+17	8.872	0.65
n-$Al_{0.6}Ga_{0.4}N$	8.9e+17	12.7	0.52
n-$Al_{0.47}Ga_{0.53}N$	2.1e+18	23.8	0.12

In order to predict the *n*-layer performance for a laser diode emitter, various *n*-layer structures for 250 nm laser diode (LD) design were explored. Figure 1 illustrates three different 250 nm LD *n*-layer designs while CTLM measurement data is presented in Fig. 2 with the

corresponding panels. The advantage of using short period superlattice (SPSL) is clearly shown as it promotes significantly better lateral current conduction. In addition, Si-doped graded buffer also enhances the electrical performance by comparing structure (b) and structure (c). Combining the observations, the final n-layer design for 290 nm LD will be described in Section 1.2.

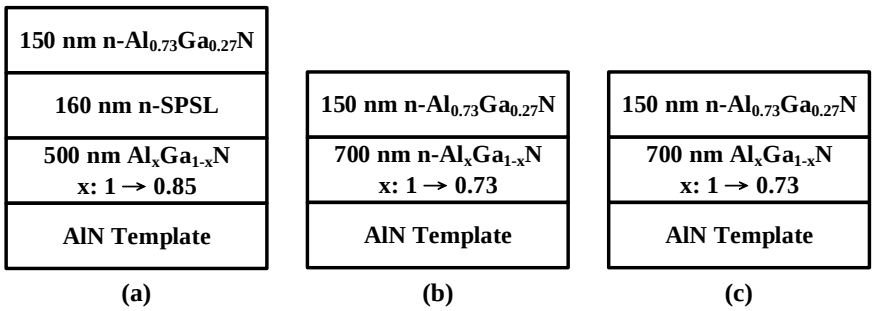

Figure 1. Various designs for 250 nm LD *n*-layers.

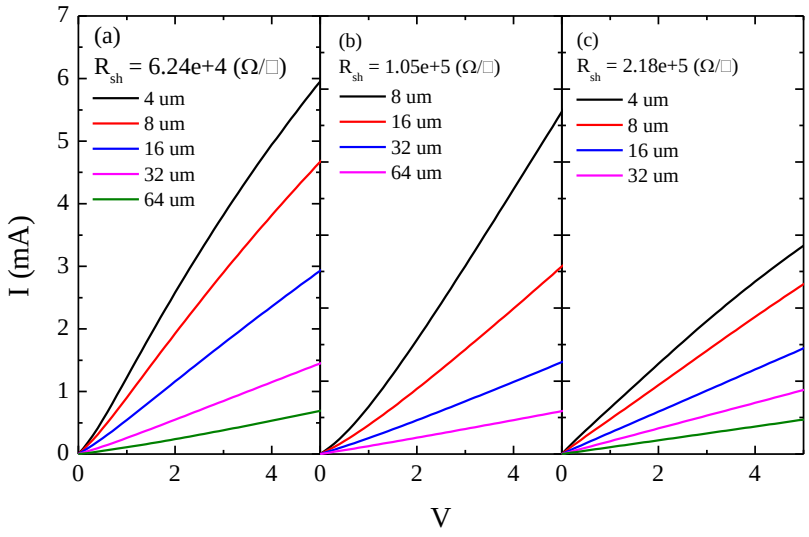

Figure 2. Circular transmission line measurements for various 250 nm LD *n*-layers.

On the other hand, obtaining the electrical characteristics for *p*-type AlGaN is not trivial since Lehighton Sheet Resistance measurement system cannot measure such high sheet resistance values while Hall measurements and CTLM measurements require *p*-type Ohmic contacts, which is difficult to achieve in AlGaN layers. Due to the compliance setting of our Hall measurement system, the resistivity is estimated by CTLM measurement when a 10V bias is applied across the contact pattern. Nickel-based metal alloy (Ni/Ag/Pt) was employed as metal contact and the estimated resistivity is summarized in Table 2.

Table 2. Summary of electrical properties from p-type AlGaN.

Sample Description	ρ (Ω·cm)
p-$Al_{0.6}Ga_{0.4}N$	18.25
p-$Al_{0.47}Ga_{0.53}N$	8.75
p-$Al_{0.4}Ga_{0.6}N$	7.25

Since Hall measurements cannot be obtained accurately, secondary ion mass spectroscopy (SIMS) on *p*-AlGaN samples was measured. Two sets of measurements were performed to predict the doping concentrations for the wide spectrum of high aluminum *p*-AlGaN. The first set of measurement studies the correlation between Cp_2Mg flow rate and magnesium concentration in the layers as shown in Fig. 3. The flow rates of Cp_2Mg were set to 600 sccm and 1000 sccm, or 2/3 of maximum flow, for the *p*-type $Al_{0.6}Ga_{0.4}N$ and the corresponding magnesium concentrations are 2×10^{19} cm^{-3} and 1.2×10^{19} cm^{-3}, respectively. Based on the magnesium concentrations and source flow rates, every 100 sccm Cp_2Mg flow provides roughly 2×10^{18} cm^{-3} of magnesium concentration; therefore, doping concentration as high as ~ 3×10^{19} cm^{-3} can be achieved at the given $Al_{0.6}Ga_{0.4}N$ growth condition.

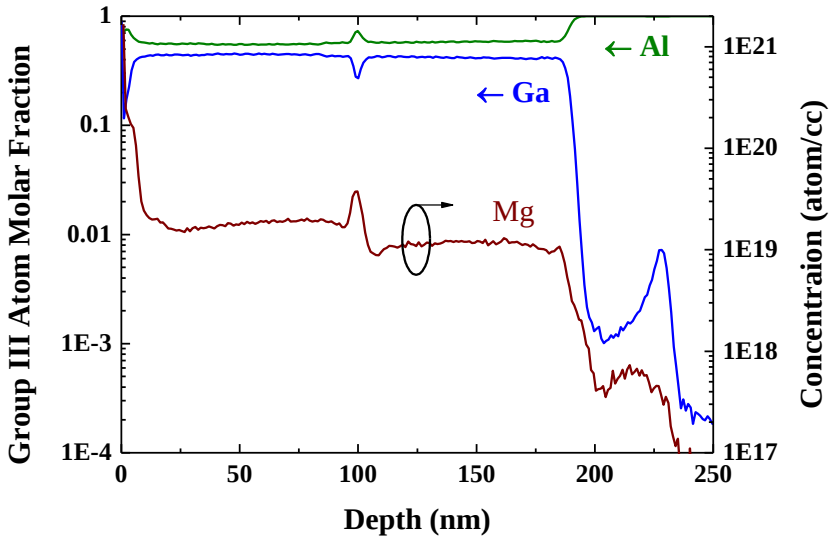

Figure 3 Secondary ion mass spectroscopy on *p*-type $Al_{0.6}Ga_{0.4}N$ with two different doping conditions.

Figure 4 demonstrated various aluminum composition AlGaN grown at a constant magnesium source flow rate (1000 sccm). Three different aluminum molar fractions, 40%, 60%, and 80%, *p*-type ternary AlGaN alloys were grown on top of AlN. Due to the difference in growth rate and V/III ratio for different aluminum molar fractions, incorporation of magnesium

varies. However, SIMS measurement suggests doping concentration above 10^{19} cm^{-3} in most of the *p*-type AlGaN alloys can be achieved.

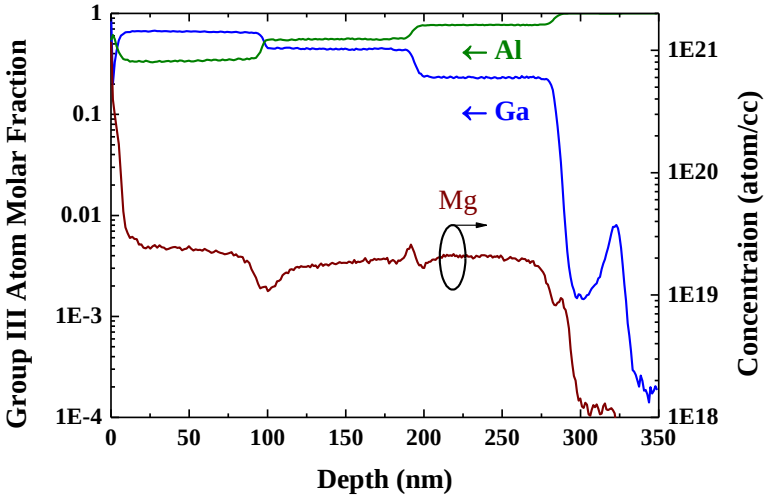

Figure 4. Secondary ion mass spectroscopy on *p*-type $Al_xGa_{1-x}N$ with constant magnesium source flow.

1.2 Prototype Laser Diode on AlN Substrate

Utilizing the achievement of the electrical conductivity of the bulk *n*-type and *p*-type AlGaN layers and the optically pumped multi-quantum well (MQW) laser (described in the interim phase II report), a laser diode prototype structure was grown on an AlN substrate. Figure 5 illustrates the cross section of a graded-index separate-confinement heterostructure (GRINSCH) MQW ultraviolet (UV) emitter. The active region consists of a four-period MQW active region structure, with 2 nm $Al_{0.32}Ga_{0.68}N$ wells and 5 nm $Al_{0.47}Ga_{0.53}N$ barriers, which under electrical excitation, is measured to emit photons with a peak wavelength of ~343 nm for the diode sample grown on AlN and ~298 nm for the diode sample grown on a sapphire substrate at the same time. Grading layers between the quantum barriers and waveguide layers are employed to enhance carrier confinement as well as optical confinement.

To confine optical mode in the transverse direction, a 500 nm thick *n*-type $Al_{0.60}Ga_{0.40}N$ layer and a 400 nm thick *p*-type $Al_{0.60}Ga_{0.40}N$ layer served as waveguide layers. In addition to the optical confinement purpose, the *n*-type waveguide layer also serves as the contact layer and the metal contact consists with vanadium-based metal alloy. Below the *n*-type contact/waveguide layer, a twelve-period SPSL with 4 nm $Al_{0.60}Ga_{0.40}N$ wells and 4 nm $Al_{0.73}Ga_{0.27}N$ barriers are used to enhance the lateral conduction and for strain relaxation management. Lastly, an *n*-type $Al_xGa_{1-x}N$ graded buffer layer with aluminum molar fraction varying from $x = 1$ to 0.73 is sandwiched between the AlN substrate and the SPSL to avoid an abrupt change in aluminum composition, which alleviates the polarization charge at the interface.

Because nickel is a lossy material in the ultraviolet spectral range, it is necessary to have the *p*-Ohmic contact far away from the optical mode to the reduce optical losses. In addition, the *p*-type contact layer needs to be low aluminum molar fraction AlGaN or GaN to avoid formation of a Schottky contact. Therefore, an inversed tapered *p*-layer design, with aluminum molar fraction

graded from 0.6 to 0, is employed to bring the *p*-type metal contact away from the optical mode and form a flat valence band between the *p*-contact layer and the active region for efficient hole transporting. The very last epitaxial layer for the laser structure is a 20 nm *p*-type GaN:Mg contact layer and the metal contact consists of a nickel-based metal alloy. Details of the fabrication process as well as the electrical and optical characteristics of the prototype laser diode emitter will be described in Task 4 below.

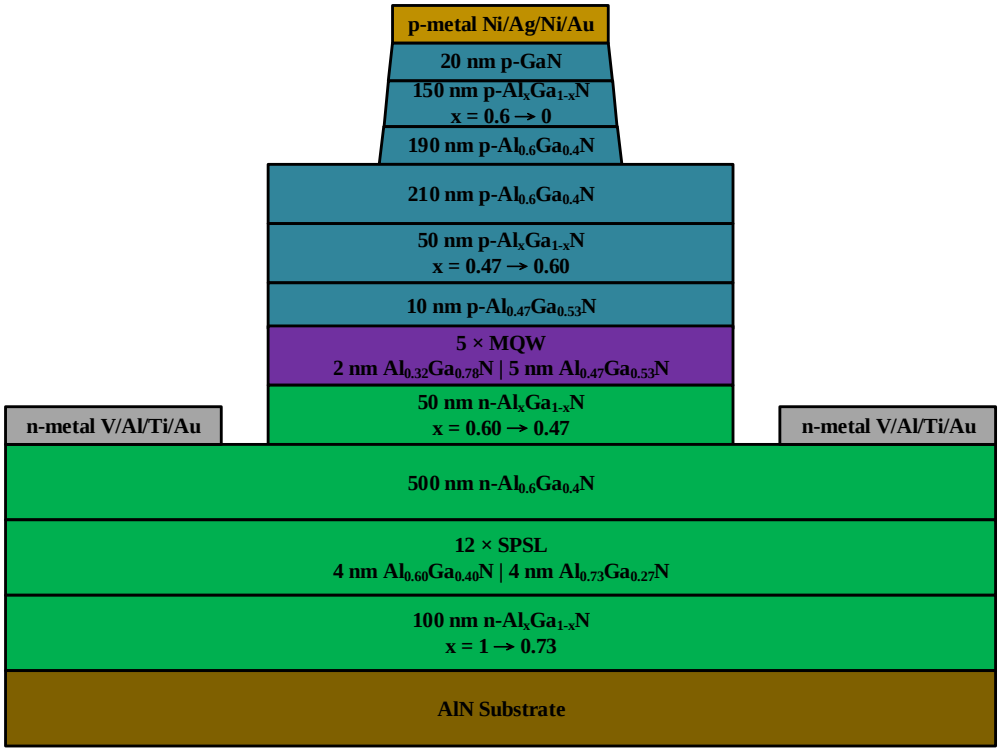

Figure 5. Schematic diagram of the inverse tapered laser diode structure on AlN template.

1.2 Development of AlGaN lasers by MOCVD in the new AIXTRON CCS System

Following the calibration of the MOCVD growth of AlGaN layers in the new AIXTRON 3x2 Close-Coupled Showerhead (CCS) MOCVD system, growth optimization of AlGaN-based MQWs was carried on AlN/sapphire templates for eventual growth on the AlN free-standing substrates. The optimized MQW structure is grown after 150 nm regrown AlN layer on the AlN/sapphire templates at 1250^{o}C, comprising 10 periods of 5 nm $Al_{0.8}Ga_{0.2}N$ barriers and 2nm $Al_{0.6}Ga_{0.4}N$ wells. Growth of the structure finishes with the last barrier layer and thus no cap layer is present.

As shown in Figure 7 (a), Photoluminescence measurements were carried to characterize the AlGaN-based MQW. The pumping power density was increased from 108 to 2570 kw/cm^2. The left figure shows a spontaneous emission spectrum with peak wavelength at 257 nm overlapped with a superluminescence emission spectrum with peak wavelength at 259.7 nm. The superluminescence becomes observable at a pumping density of 632 kW/cm^2. The linewidth of the superluminescence emission is 2 nm and it is TE polarized.

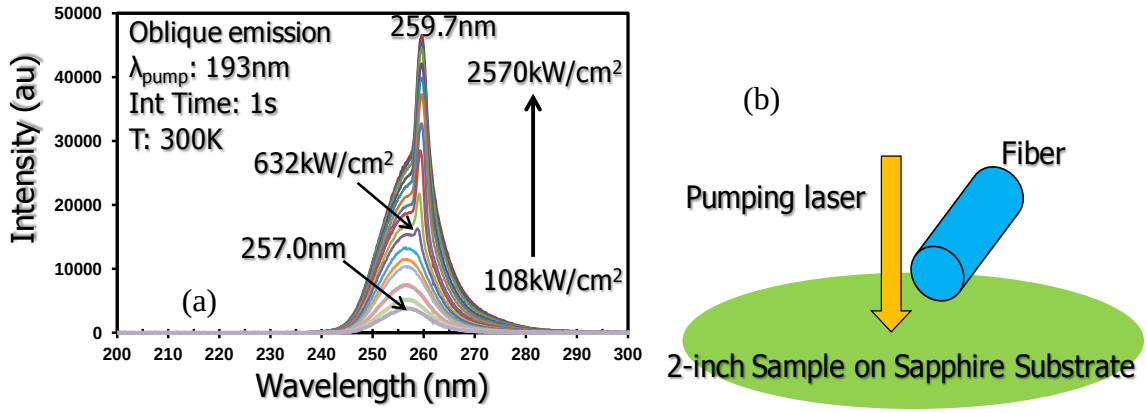

Figure 6. (a) PL spectra of surface emission from optimized AlGaN-based MQW grown on AlN/sapphire templates at 1250°C; (b) Experimental setup of PL measurement.

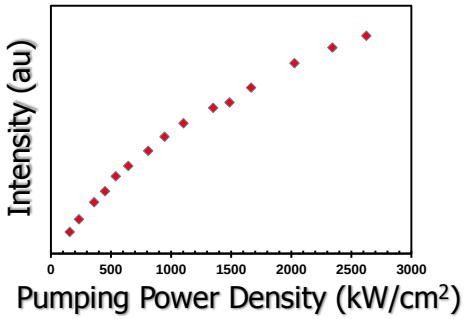

Figure 7. Integrated intensity of PL spectra of the surface emission as shown in (a) as a function of pumping power density.

We note that the spontaneous emission and superluminescence presented here are not from a laser cavity. Rather, it is obtained by vertically photo-pumping a 2-inch dia. sample. The emission is collected by an optical fiber at about 60 degrees with respect to the sample surface. Due to the lack of laser cavity, there is no abrupt increase in the curvature of *I-P* curve as shown in Figure 7. The curvature slightly decreases at high pumping density due to difficulty in heat dissipation on the sapphire substrate. Therefore no pumping threshold has been extracted.
To our knowledge, the study represents the superluminescence with lowest wavelength from AlGaN-based MQWs on the sapphire substrate. Since superluminescence is the spontaneous emission amplified by stimulated emission in the gain medium, this study demonstrates the excellent candidacy of AlGaN-based MQWs grown at 1250°C for lasing.

In addition to PL measurements, we have carried transmission electron microscopy (TEM) experiment on the AlGaN QWs. As seen from the left Figure 8 (a) and (b), sharp QW/QB interfaces have been observed and all the ten wells are present. The thickness of the well and barrier are 2.1nm and 5.6nm, respectively, which meets our design. In addition, atomic force microscopy (AFM) image on the right shows a smooth surface with roughness of 0.3nm.

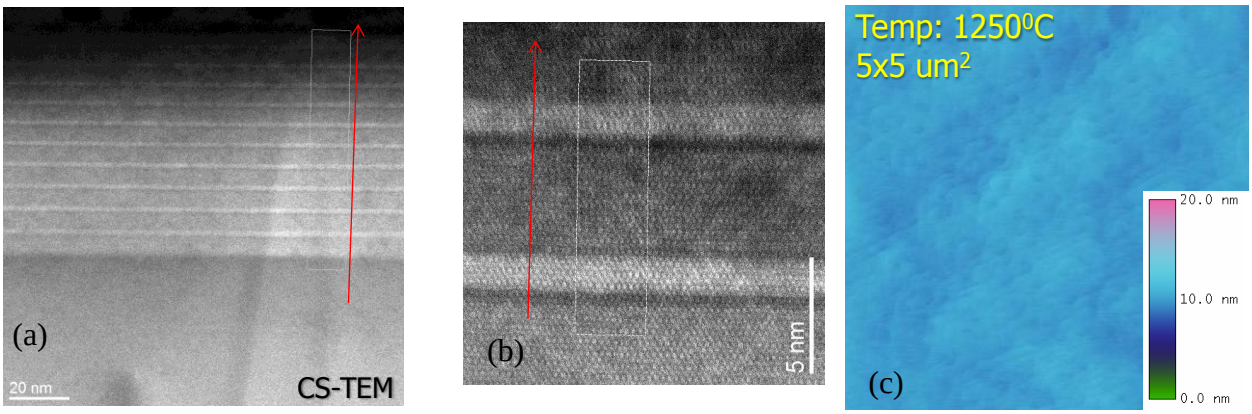

Figure 8. (a) Cross-sectional TEM, (b) high-resolution TEM and (c) AFM images of optimized AlGaN-based MQW grown on AlN/sapphire templates.

1.3 Development of AlGaN-based MQWs on AlN Substrate in F4

Following the growth optimization of AlGaN-based MQWs on AlN/sapphire templates, we have grown the AlGaN-based MQW on AlN free-standing substrates (MQW/AlN wafer) to take advantage of its low defect density and homoepitaxy. As shown in Figure 9, a 115-nm high-temperature AlN buffer layer was grown at 1300°C on the AlN substrate, followed by a strain-relief interlayer and a waveguide layer. An active region comprising eight periods of 2-nm $Al_{0.60}Ga_{0.40}N$ quantum wells and 5-nm $Al_{0.78}Ga_{0.22}N$ quantum barriers was grown directly on the waveguide layer at 1250°C. To further enhance the Al-adatom mobility, low V/III ratios were individually optimized for the high-temperature AlN buffer layer (20) and AlGaN-based MQW structure (50-100), which was found to promote two-dimensional growth and smooth surface formation.

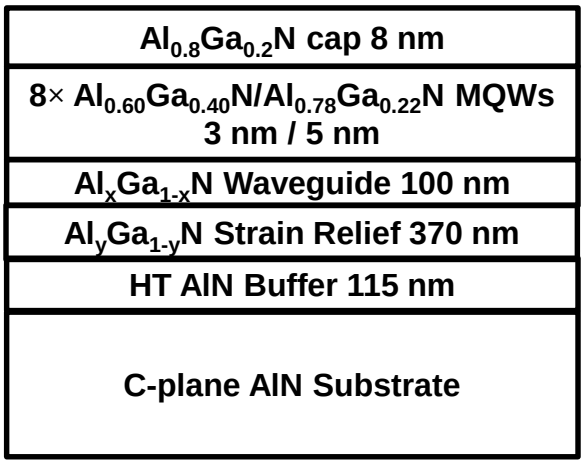

Figure 9. Schematic diagram of MQW structure optimized for optical pumping experiments.

To obtain high-quality AlGaN-based MQWs, active regions on the AlN substrate were grown using intentional interruption between switching the growth conditions of the QW and QB. As the NH_3 flow rate was dramatically different between growth conditions for the QW and QB due to the different V/III ratios, it was found that the NH_3 ramping time between the growths of QW and QB is influential on the luminescence characteristics. The zero or shorter ramping time can lead to a transient in the NH_3 flow rate, which resulted in uncontrollable inhomogeneity of

material compositions and thus large FWHM of the emission spectrum. On the other hand, longer ramping times caused a larger surface roughness due to the AlGaN decomposition at the high growth temperature. In this study, we have found that the deposition/decomposition rate of the given compositions of AlGaN material is very sensitive to the temperature around 1250^{o}C. Thus an emission wavelength shift can occur with an unstable growth temperature. Eventually, a ramping time of 2.5s from well to barrier and barrier to well growth was found to be optimal. The whole structure on the AlN substrate is finished with a thin cap layer of $Al_{0.78}Ga_{0.22}N$ for surface passivation. It is noted that an increased thickness of cap layer could increase the transverse optical confinement of the entire active region. However, a thicker cap layer leads to higher absorption loss of excitation power of the 193-nm excimer pump laser, limiting the cap layer to be thin.

As shown in **Figure 10**, the room-mean-square (RMS) roughness of MQW/AlN wafer is 0.11 nm. Terraced step flow is preserved, which is a characteristic of two-dimensional epitaxial growth. Considering that prior to growth, AlN substrates typically possess RMS roughness of 0.25 nm and 0.05-0.10 nm, respectively, the growth of the MQW structures indicate a slight surface roughening while maintaining a low defect density thanks to the higher adatom mobility at high temperature.

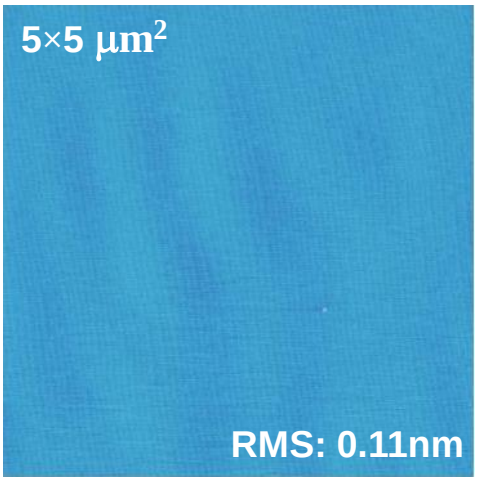

Figure 10. AFM images of AlGaN-based MQW grown on AlN substrates.

Asymmetric (105) reciprocal space mapping (RSM) of the MQW/AlN wafer by high-resolution triple-axis X-ray diffraction was conducted. As shown in **Figure 11**, the entire structure is pseudomorphically deposited on the AlN substrate. To study the lasing characteristics of the MQW/AlN wafer, the wafer was thinned to 80 um by lapping the AlN substrate and a Fabry-Perot cavity was formed using cleaved m-plane facets with a 1.05-mm long resonant cavity. The laser bars were optically pumped by the 193-nm excimer laser in edge-emission configuration at room temperature.

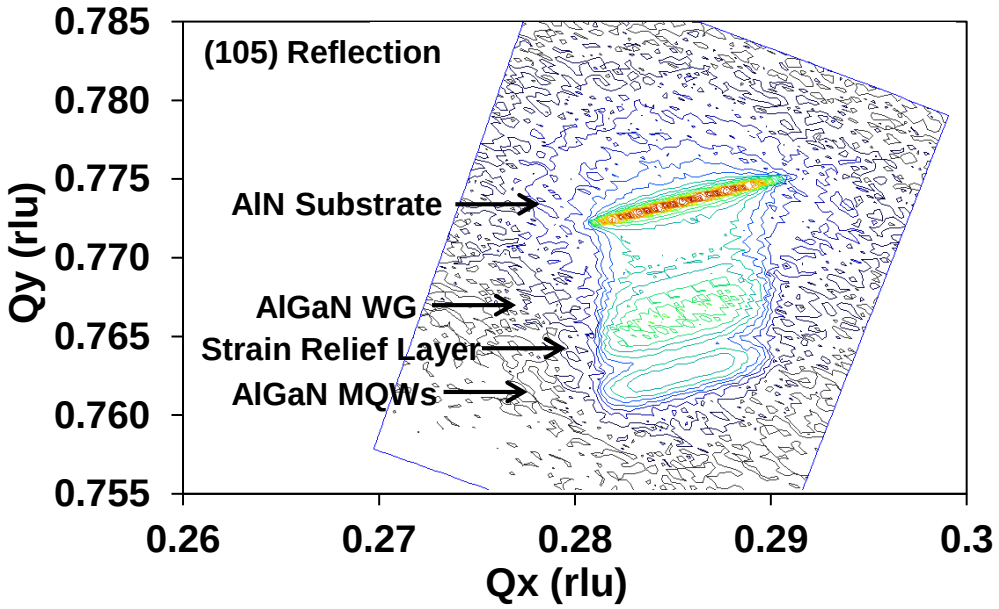

Figure 11. X-ray diffraction reciprocal space mappings of MQW/AlN wafer in Figure 10.

Laser emission spectra with different pumping power densities are shown in Figure 20. The peak wavelength of spontaneous emission was 268.2 nm with FWHM of 7.52 nm at the minimum measured pumping power density of 35 kW/cm^2, while the peak wavelength of laser emission was 266.0 nm with FWHM reducing to 0.91 nm at the maximum measured pumping power density of 192 kW/cm^2. The laser emission band is located on the high-energy slope of the spontaneous emission spectrum. Localized states and screening of the built-in electric field have been attributed to the blue shift of the laser emission band.[3] As shown in **Figure 12**, the pumping power density dependent spectral integrated intensity demonstrates a distinct lasing threshold at the pumping power density of 124 kW/cm^2. Beyond the threshold the laser emission output increases linearly with the pumping power density. The threshold is similar to the threshold of 126 kW/cm^2 at peak wavelength of 267 nm reported in the recent study, which utilized slightly different approach to estimate the lasing threshold.[4] The threshold could be further reduced by growing thicker cap layer to increase the optical confinement within the active region and/or using excitation source with longer wavelength to reduce absorption in the non-QW layer.

In addition, the polarization of the laser emission was determined at pumping power density 1.9 times higher than the threshold. As shown in the inset of Figure 12, the laser emission is TE (perpendicular to *c*-axis) dominant with the degree of polarization, defined as (I_{TE} - I_{TM})/(I_{TE} + I_{TM}) equals 0.91, which is desired for edge-emitting lasers due to less penetration of beam profile into lossy regions vertically as compared to transverse magnetic (TM) polarization (parallel to c-axis). This observation is consistent with the previous experimental and theoretical studies and suggests dominance of topmost valence band transition based on heavy holes (TE polarization) over split-off holes (TM polarization) with the given or similar growth conditions in the reported wavelength range.

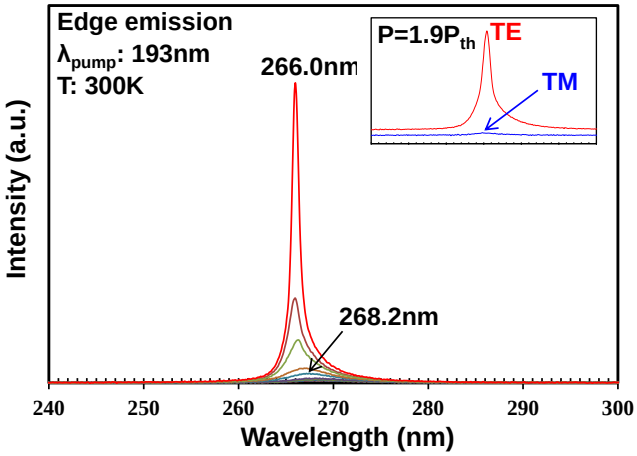

Figure 12. The laser emission spectra of AlGaN-based MQW on the AlN substrate with pump power densities below and above threshold at room-temperature. The inset shows TE and TM-modes emission spectra for the same laser bar operating above threshold at room-temperature.

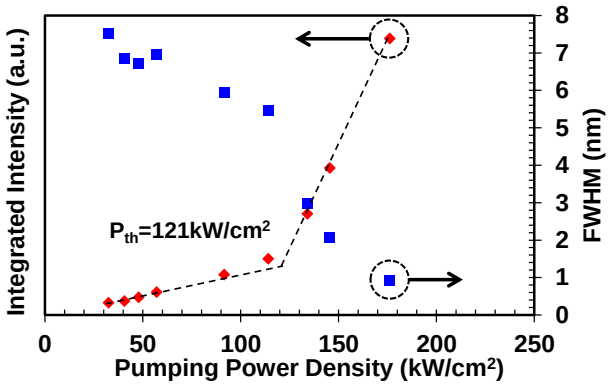

Figure 13. Integrated spectral intensity and FWHM of the laser emission spectra of AlGaN-based MQW on the AlN substrate as a function of the optical pump power density at room-temperature.

In summary, lasing at 266.0 nm was demonstrated with threshold of 124kW/cm^2 from AlGaN-based MQWs on the AlN substrate at room temperature. The threshold can be further reduced by employing thicker cap layer and/or excitation source with longer wavelength. These results demonstrate viability of high temperature growth for high-quality active region for future development of UV-C laser diodes

TASK 2: Detailed III-N Materials Characterization

2.1 Main Activities

The ASU team was tasked with detailed analysis of QW structures for short wavelength UV emitters: Structural analysis using high resolution TEM (HRTEM), and high-angle annular dark-field modes (HAADF); Optical characterization using cathodoluminescence (CL) spectroscopy and imaging; Compositional profiling using Rutherford backscattering spectroscopy (RBS) and HAADF.

Summary of Achievements:

RBS measurements performed on InAlN layers determined the existence of unwanted gallium atoms (contaminants). We found that gallium was adhering on the reactor walls and desorbing during growth (Fig 1(a)). Figure 1 (b) shows InAlN layers with Ga content up to 15%. **Silicon doping did not affect the quaternary alloy composition. But increasing the magnesium flow reduced indium incorporation.**

(a) (b)

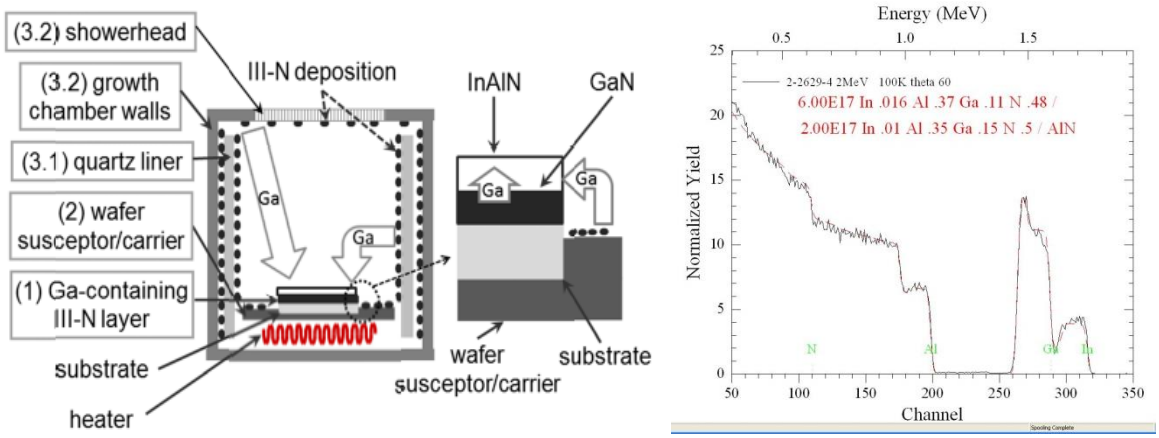

Fig. 1. (a) Schematic view showing possible sites leading to Ga auto-incorporation in a growth chamber with a close-coupled-showerhead. (b) Example of an RBS spectrum of an unintentionally grown InAlGaN layer.

We have observed that AlGaN-based QWs grown on sapphire exhibit an inhomogeneous QW emission. This emission depends on the impurity incorporation in the underlayer. Room temperature CL spectra shows a sharp QW emission at 267 nm in Figure 2(a). The bright spots of the monochromatic image in Fig. 2(b), taken at the left shoulder of the 267-nm emission, corresponds to regions of lower gallium content. We also observe that an impurity-related luminescence, Fig. 2(d), has the same contrast as Fig 2(b), suggesting that gallium preferably gets incorporated in regions where the impurity is not located. **More gallium incorporation in regions where there is less impurity incorporation in the underlayers.**

We studied the effect of cap layer thickness on QW emission of AlGaN-based MQWs grown on sapphire. Figure 3(a) shows the AlGaN MQW structure with a 20-nm-thick cap layer, whereas Fig. 3(b) shows a similar structure with a 350-nm-thick cap layer. The layers were grown under the same conditions. Figure 3(c) shows a room temperature CL spectrum of film with the 20-nm thick cap layer. The QW emission is centered at 263 nm. Figure 3(d) shows a CL spectrum of the film with the 350-nm cap layer. The emission is now centered at 258 nm, 5 nm blue shifted from the other structure. We believe that **a thicker cap layer may have screened the spontaneous polarization charges and thus do not contribute to the total internal field in the QW layer. Therefore, a blue shift in the emission wavelength is observed.**

(a)

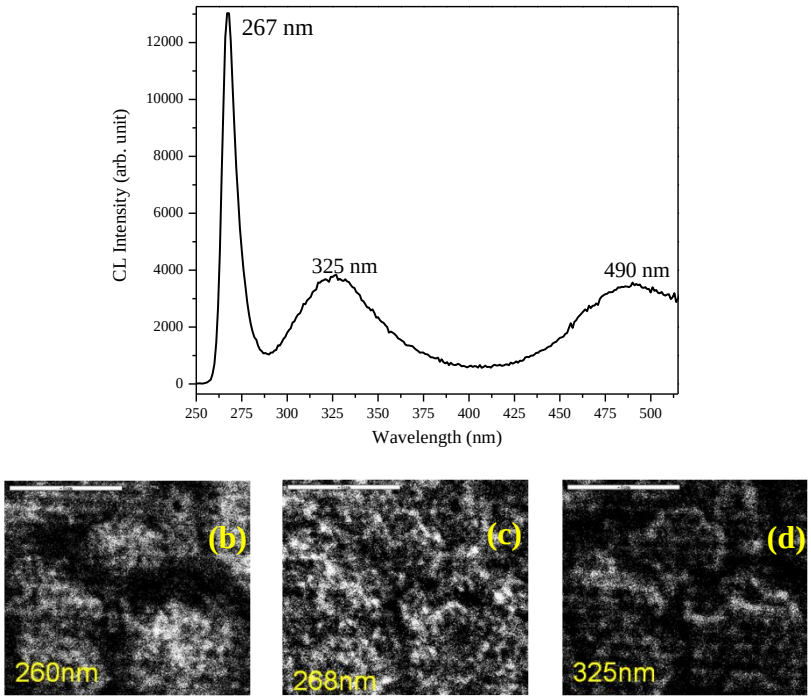

Fig. 2. (a) Room temperature CL of an AlGaN MQW structure. (b-d) Monochromatic images taken across the spectrum.

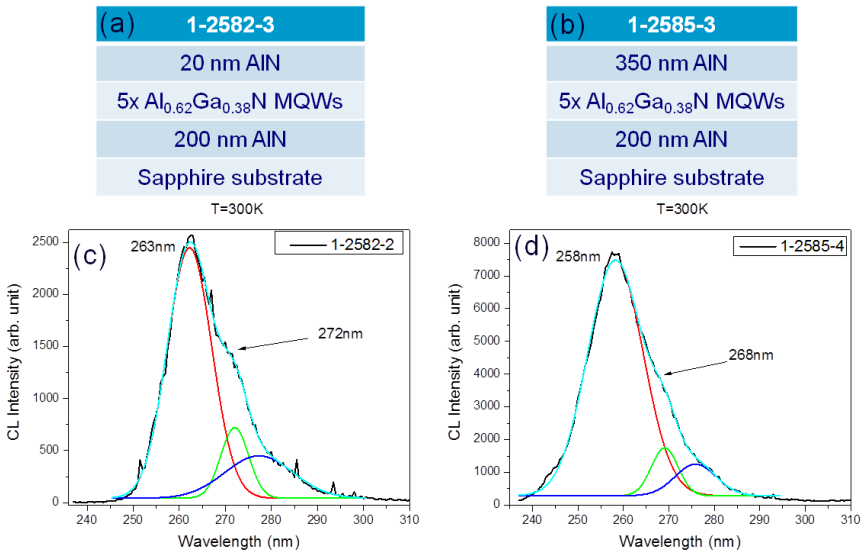

Fig. 3. Sample structure of an AlGaN MQW structure with (a) 20-nm- and (b) 350-nm-thick cap layer. (c) and (d) are the corresponding CL spectra of (a) and (b) structures. The QW emission of (b) is blue shifted by 5 nm with respect to (a).

We have studied the effect of the number of trimethylgallium (TMGa) sources on the growth of AlGaN MQWs: one TMGa (or interrupted growth) leads to the formation of Al-rich

(a) (b)

monolayers at the QW/QB interfaces. This feature disappears when two TMGa sources (continuous growth) are used.

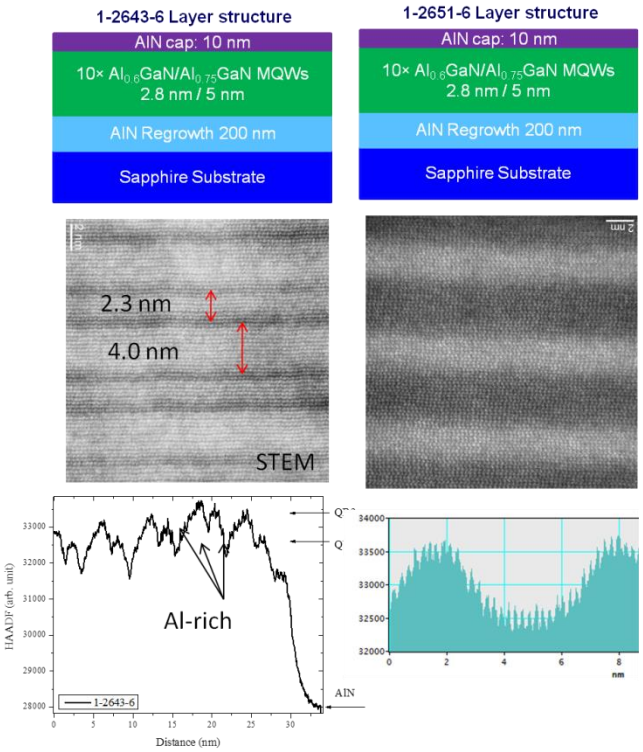

Fig. 4. AlGaN MQW structure grown with (a) one and (b) two TMGa sources. Al-rich monolayers appear at each QW/QB interface when one TMGa is used. The problem is fixed in (b). The HAADF graphs in the bottom show the difference of the Al content across the active region between these two samples.

We have observed lasing action in AlGaN-based QWs with Al-rich monolayers at QW/QB interfaces observed by cathodoluminescence. PL measurements showed lasing modes at 225nm. By increasing the beam current and magnification, we can increase the current density up to a factor of five. At low current densities (Fig. 5), the QW emission is broad. As we increase the current density, a sharp peak appears and becomes dominant. The full-width-at-half-maximum is ~ 1nm and the emission peak is ~ 228nm.

We have also studied the effect of substrate choice on the optical properties of AlGaN QWs: Highly luminescent and uniform QW emission is observed in samples growth on AlN (Fig. 6(a)), possibly due to superior material quality (absence of abrupt incoherent AlN/sapphire interface). The use of a sapphire substrate leads to spotty and low intensity emission, as shown in Fig. 6(b). **The aluminum content in the QWs is reduced (observed by STEM and CL peak emission) possibly due to lower thermal conductivity of sapphire (23.1 W/mK) with respect to AlN (285 W/mK).**

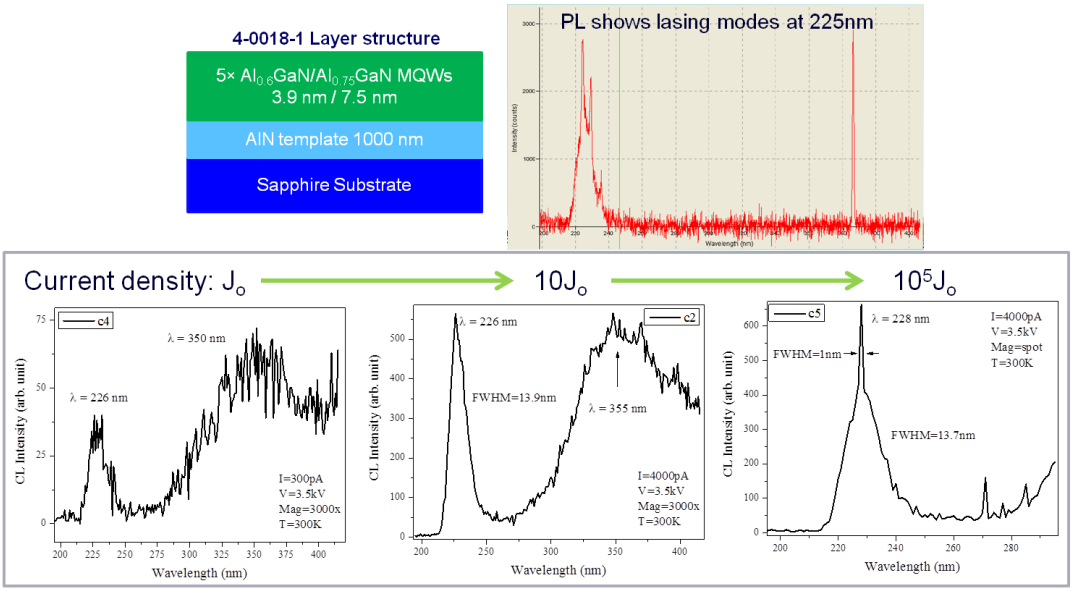

Fig. 5. AlGaN MQW structure exhibiting lasing action measured by PL and CL at room temperature.

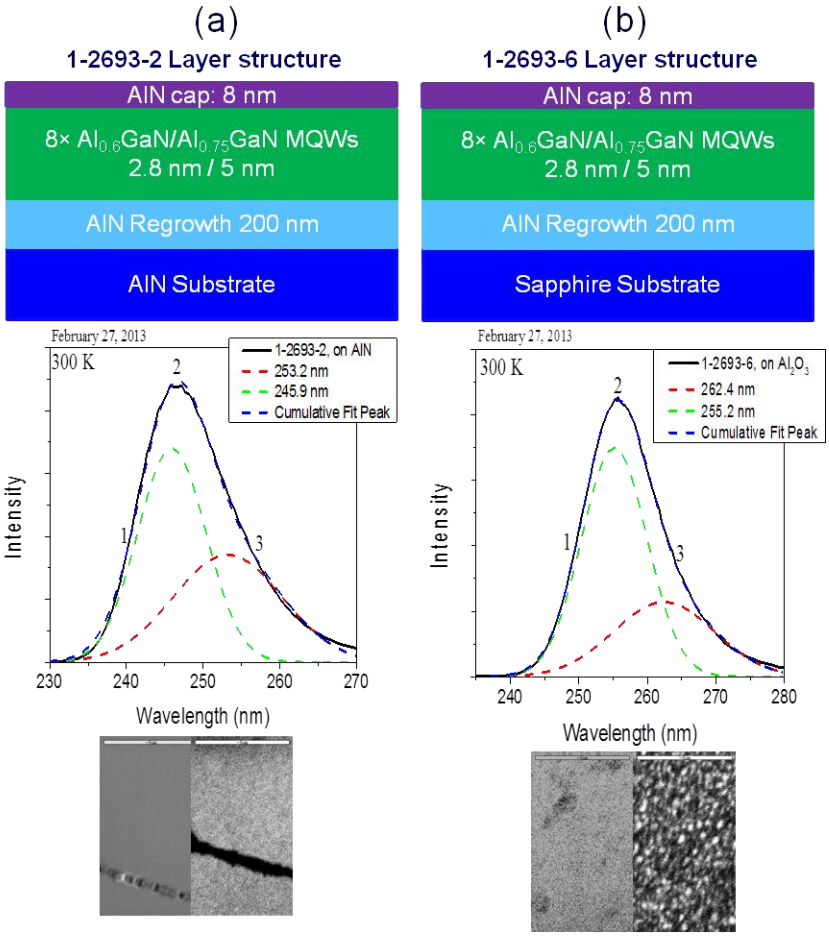

Fig. 6. Comparison of the optical properties of AlGaN MQWs grown on (a) AlN and (b) sapphire substrates. CL spectra shows a MQW emission at (a) 245.9 and (b) 255.2 nm. The figures in the bottom represent the SE and monochromatic CL images of the QW emission.

TASK 3: III-N UV Laser Design and Simulation

We have applied advanced numerical techniques for the simulation of semiconductor laser diodes (LDs) to (1) investigate the influence of both microscopic material properties and device design parameters on macroscopic device performance; (2) identify and quantify factors limiting device performance; and (3) suggest strategies for optimization of ternary- and quaternary-based laser diode design.

A plethora of practical issues complicate the design of high-power ~250 nm edge-emitting LDs, of which the most severe is arguably efficient *p*-type doping. Specifically, the high activation energy of Mg acceptors in wide-bandgap III-Nitride alloys places constraints on the electrical conductivity of *p*-type material, leading to challenges in the formation of *p*-Ohmic contacts, parasitic series resistance, Joule heating, and even hole injection into the active region. The use of narrower-bandgap AlInGaN materials to ensure higher *p*-type conductivity is not an appealing alternative due to both a reduction in optical confinement as well as the introduction of severe absorption loss. Inefficient *p*-type doping furthermore renders perfectly symmetric optical waveguides non-optimal, as asymmetry becomes necessary to maximize the overlap of the lasing mode(s) with the active region, yet minimize this overlap with the *p*-Ohmic metal. A third major challenge originates from the polar nature of wurtzite III-N materials, as spontaneous and piezoelectric polarization charges in polar III-N materials are well known to induce large built-in electric fields that reduce the overlap between electron and hole wave function within QWs. Moreover, the Yoder group at Georgia Tech has previously demonstrated that unscreened polarization charges are responsible for the formation of parasitic inversion layer of electrons and artificial hole blocking layer at the *p*-side. Our efforts to date towards the realization of high-power CW LDs operating at 250nm include several innovative ideas which have been presented at program reviews and documented in three journal publications with an additional one under development. A brief summary of our principle results is provided below.

AlInN based DUV LD design:

Early in the CMUVT program, we theoretically demonstrated a prototypical 250 nm UV LD design based exclusively on AlInN ternary material as a promising alternative to AlGaN-based designs, for applications in the UV-C band [1]. AlInN offers a new and promising alternative to AlGaN for the realization of optoelectronic devices operating in the UV-C band in terms of bandgap and waveguide design, yet has received relatively little attention in the literature. One of the major bottlenecks in short wavelength UV LD design is the poor conductivity of p-type layers. Alloying InN with AlN may improve the dopant ionization efficiency because Mg has a very low ionization energy in InN (~60 meV) [2].

We have explored a rich design parameter subspace by means of numerical simulation to achieve minimum threshold current and maximum slope efficiency for an AlInN/AlInN LD design, and proposed the epitaxial layer structure detailed in Table 1. The LD structure is assumed to be 650 μm long with a mesa width of 10 μm. The cross-sectional area of the p-contact is 6.5×10^{-5} cm^2, and the entire structure is assumed to be pseudomorphically grown on top of a c-axis AlN substrate. Two-dimensional calculations predict good optical confinement (~1.0%) for LD stripes formed by etching to a depth of 0.61 μm, or 100 nm above the top surface of the EBL. Our numerical investigation revealed that designs featuring homogeneous EBL layers exhibit a parasitic inversion layer of electrons as a consequence of strong interfacial

polarization charge, resulting in a degradation of device performance through enhanced nonradiative recombination. Instead, volumetric redistribution of polarization charge by means of a tapered EBL layer was shown to completely suppress the formation of a parasitic inversion layer without any undesirable consequences, and lead to lower threshold current.

Table 1: Epitaxial layer structure for an AlInN/AlInN LD design operating at 250 nm. EBL and N-cladding (inner) layer compositions are graded to redistribute interfacial polarization charge over their entire thickness.

Layer Name	*Material*	*Thickness (nm)*	*Refractive index*
Contact	GaN	10	2.3
P-cladding (Outer)	$AlIn_{0.05}N$	600	2.1875
P-cladding (Inner)	$AlIn_{0.10}N$	100	2.225
EBL	$AlIn_{0.12\sim0.07}N$	10	2.24 ~ 2.2025
Spacer	$AlIn_{0.12}N$	4.0	2.24
QW	$AlIn_{0.17}N$	2.0	2.2775
QWB	$AlIn_{0.12}N$	4.0	2.24
N-cladding (Inner)	$AlIn_{0.10\sim0.12}N$	100	2.225 ~ 2.24
N-cladding (Outer)	$AlIn_{0.05}N$	600	2.1875
Buffer	$AlIn_{0.03}N$	1000	2.1725
Substrate	AlN	-	2.15

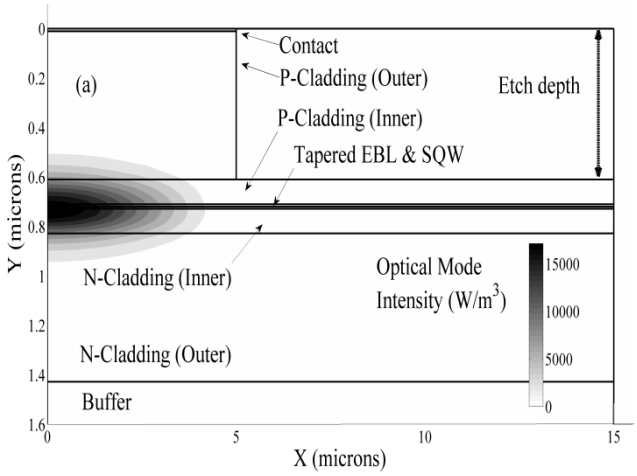

Figure 1. Optical mode profile corresponding to the epitaxial structure of Table 1 (Only the fundamental TE mode is shown here).

A comparison of L-I and V-I curves for two LDs featuring tapered and uniform EBL designs is provided in Figure 2, from which it is evident that the tapered design results in an 8% reduction in threshold current, a 4% reduction in threshold voltage and a 20% increase in slope efficiency. The uniform EBL design compared here has the same dimension and epitaxial structure of that of tapered EBL design (Table 1) except that homogeneous $Al_{0.93}In_{0.07}N$ material is used for the EBL.

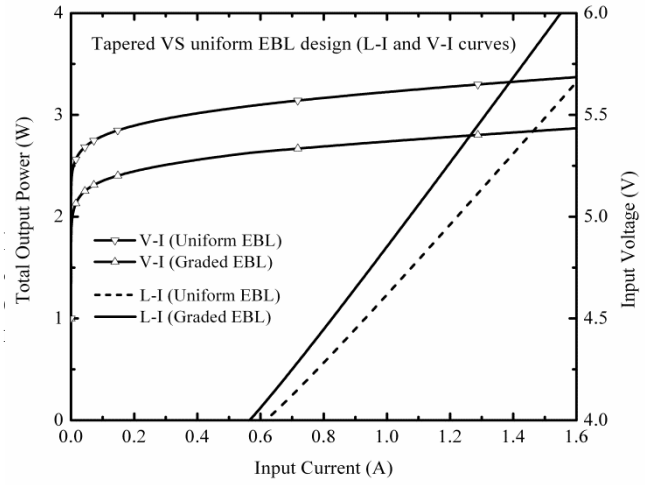

Figure 2. Comparison of L-I and V-I curves between tapered and uniform EBL design. Tapered design yields an 8% reduction in threshold current, a 4% reduction in threshold voltage and a 20% increase in slope efficiency.

Band diagrams (above lasing threshold) and carrier densities for both the tapered and uniform EBL designs are provided in Figure 3, demonstrating the efficacy of the tapered EBL design in suppressing the formation of a parasitic inversion layer. Although the barrier height of tapered EBL is reduced at the spacer/EBL interface, it is sufficiently large at the other interface to block electron leakage from the active region.

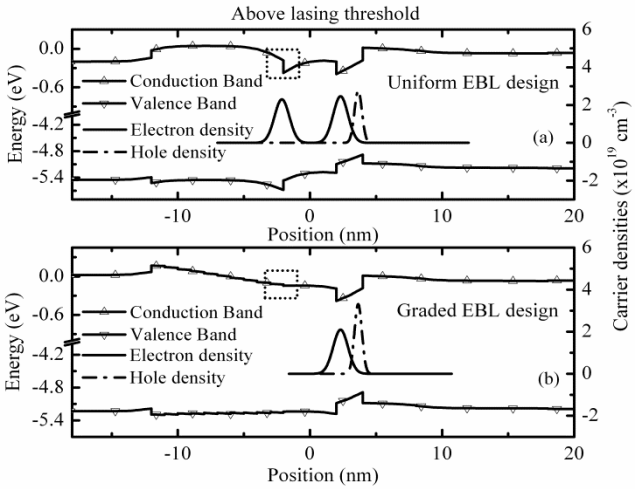

Figure 3. Energy band diagrams (above lasing threshold) and carrier densities of uniform (a) and graded (b) EBL design. Parasitic inversion layer charge is completely removed in (b) without any undesired side effects.

In order to suppress the parasitic inversion layer at the EBL/spacer interface, we have investigated LD designs with a variety of EBL and spacer layer attributes. Our simulation results suggest that unlike other alternatives, the tapered EBL design eliminates the parasitic inversion layer without any undesirable side effect.

Lowering the indium content of the spacer layer or increasing that of the EBL may reduce the lattice mismatch between these two layers, and thus minimize the net interfacial polarization charge. Figure 4 demonstrates that a reduction of spacer layer indium content improves both threshold current and slope efficiency. As expected, this is attributable to a reduction in lattice mismatch, and leads consequentially to the reduction of net polarization charge at the EBL/spacer interface. But there is a problem with this approach: net polarization charge at the lower spacer layer interface increases, plunging the quantum well conduction band downwards in energy relative to the quasi-Fermi level. This may not only reduce the electron-hole overlap in QW, but also influence lasing wavelength as well. Similarly, indium rich EBL designs also reduce threshold current and improve slope efficiency (see Figure 5). An undesirable side-effect of this design strategy, however, is a reduction in barrier height, compromising the effectiveness of this layer to block the leakage of injected electrons from the active region.

In addition to the indium content of the spacer and EBL layers, we have also investigated whether a change in their respective thicknesses may help suppress parasitic inversion layer charge. Our simulations indicate that thicker EBL and spacer layers only slightly improve salient features of the L-I curve, but that the problem of a parasitic inversion layer persists. In theory, highly conductive spacer layers can narrow the physical extent of the parasitic inversion layer.

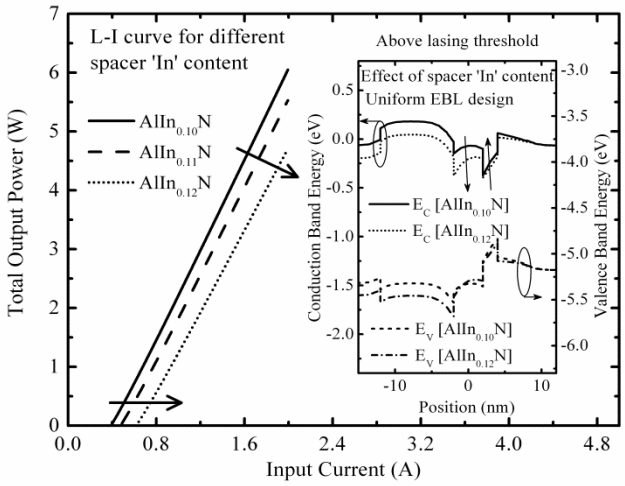

Figure 4. L-I curves for different spacer In content. Inset figure shows how energy band diagrams (above lasing threshold) change with spacer In mole fraction. Lowering spacer In content may eliminate parasitic inversion layer but as a side effect, it modifies the energy band diagram of the SQW.

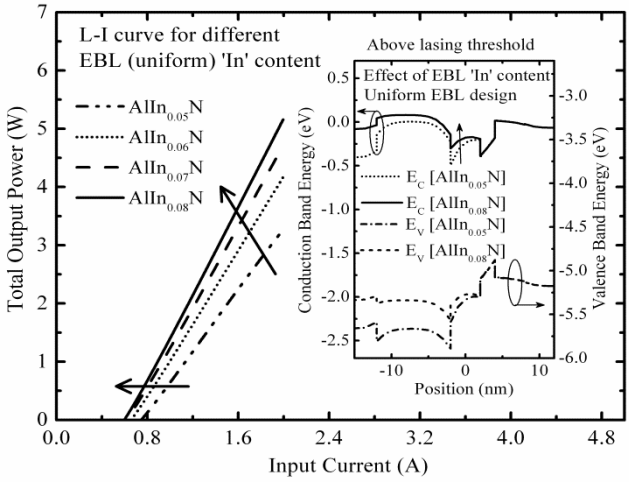

Figure 5. L-I curves for different EBL indium content. Inset figure shows energy band diagrams (above lasing threshold) for two different EBL indium mole fractions. An undesired consequence of this approach is the reduction of EBL barrier height.

Although Figure 6 shows signs of improvement in both threshold current and slope efficiency, in practice, this improvement will be limited by the reduction of minority carrier lifetime, an effect which is not considered to simulate L-I curves of Figure 6. Besides, high activation energy of Mg dopants makes the realization of sufficiently large free hole concentrations challenging in heavily doped p-type AlInN for present purposes.

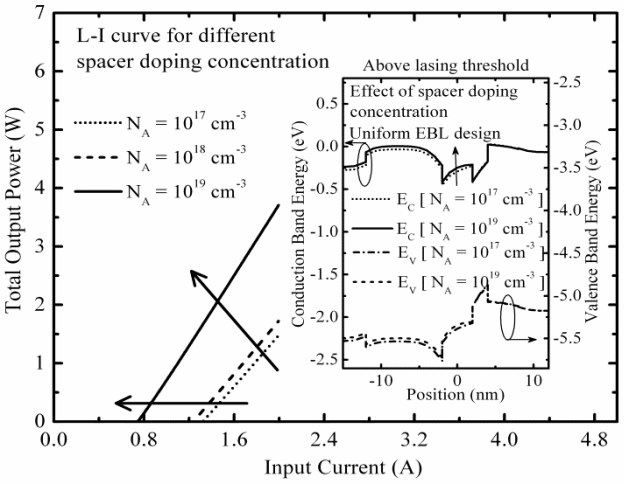

Figure 6. L-I curves for different spacer doping concentration. Inset figure shows energy band diagrams (above lasing threshold) for two different doping concentrations of spacer. Higher activation energy of P-type dopant makes it difficult to achieve highly conductive AlInN layers.

It is evident that design strategies to eliminate parasitic inversion layer charge, presented in Figs. 4-6 either comes with undesirable side effects or they are challenging for practical implementation. The main reason of the parasitic inversion layer charge is the existence of a large net polarization charge at the EBL/spacer interface. Linearly tapering of EBL material composition, however, affects a redistribution of this interfacial polarization charge over the entire volume of the EBL layer, suppressing the formation of any parasitic inversion layer without penalty to electron barrier height.

Polarization charge matched DUV LD design:

Epitaxial growth of AlInN with superior crystalline quality poses unique challenges arising from the disparity in optimum growth temperature between AlN and InN. As a consequence, we shifted our immediate research focus to design an LD based primarily on AlGaN ternary materials. We have proposed polarization matching as a strategy for enhancement of wavefunction overlap in active regions, and demonstrated significant improvement in threshold current and slope efficiency with our numerical simulations [3]. In our approach, AlInGaN quaternary barrier compositions are chosen judiciously to eliminate net polarization charge at barrier/well interfaces. Although the use of polarization-charge-matched quaternaries has already been proposed in the literature to improve performance of visible wavelength LEDs and LDs, reference [3] presents the first demonstration that this is also feasible for DUV LDs operating at sub-300 nm wavelengths. Our overlap-enhanced LD designs can easily take advantage of thicker QWs to enhance both optical confinement factor and optical matrix element. Polarization-matched quaternary barriers offer an additional degree of freedom to tune QW depth in the conduction and valence bands, a feature that can be used to increase carrier capture efficiency. Margin of error analysis revealed that even a partially suppressed interfacial polarization design is appreciably superior to designs using exclusively ternary AlGaN barriers.

The proposed epitaxial layer structure (shown in Table 2) is optimized using numerical simulation to achieve minimum threshold current and maximum slope efficiency. It is assumed that all layers are pseudomorphically grown on top of an AlN substrate. The EBL is compositionally graded from $Al_{0.794}In_{0.065}Ga_{0.141}N$ (bottom) to $Al_{0.85}Ga_{0.15}N$ (top) to redistribute the polarization charge volumetrically. N-waveguiding layer went through similar tapering for the same reason. Two-dimensional calculations (see Figure 7) predict good optical confinement (~2.2%) for 650 μm edge-emitting LD stripes formed by etching to a depth of 0.61 μm, or 100 nm above the top surface of the EBL. Ridge width is 10 μm and cavity length is 650 μm. Left and right facet reflectivities are assumed to be 85% and 95%, respectively. No background optical loss is considered in our simulations.

Table 2: Epitaxial layer structure for an AlGaN/AlInGaN edge emitting LD design operating at 250 nm. EBL and N-waveguiding layer compositions are graded to redistribute interfacial polarization charge over their entire thickness.

Layer Name	Material	Thickness (nm)	Refractive index
Contact	GaN	10	2.3
P-cladding	$AlGa_{0.15}N$	600	2.1725
P-waveguiding	$AlGa_{0.20\sim0.15}N$	100	2.18 ~ 2.1725
EBL	$AlIn_{0.065\sim0.0}Ga_{0.141\sim0.15}N$	40	2.22 ~ 2.1725
Spacer	$AlIn_{0.065}Ga_{0.141}N$	3.0	2.22
QW (×3)	$AlGa_{0.465}N$	2.0	2.2197
QWB (×3)	$AlIn_{0.065}Ga_{0.141}N$	3.0	2.22
N-waveguiding	$AlIn_{0.0\sim0.065}Ga_{0.15\sim0.141}N$	100	2.1725 ~ 2.22
N-cladding	$AlGa_{0.15}N$	600	2.1725
Buffer	$AlGa_{0.10}N$	1000	2.165
Substrate	AlN	-	2.15

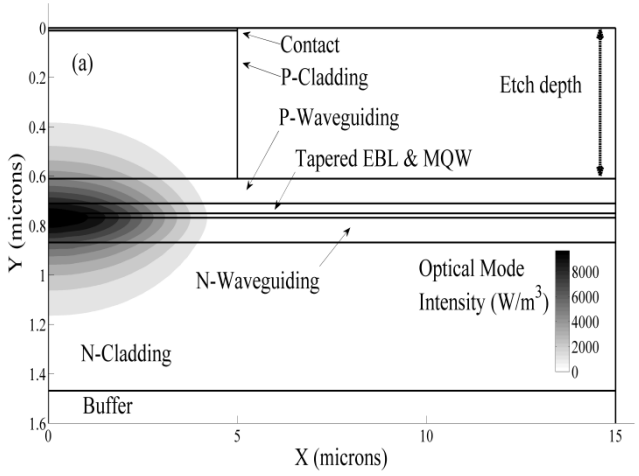

Figure 7. Optical mode profile corresponding to the epitaxial structure of Table 2 (Only the fundamental TE mode is shown here).

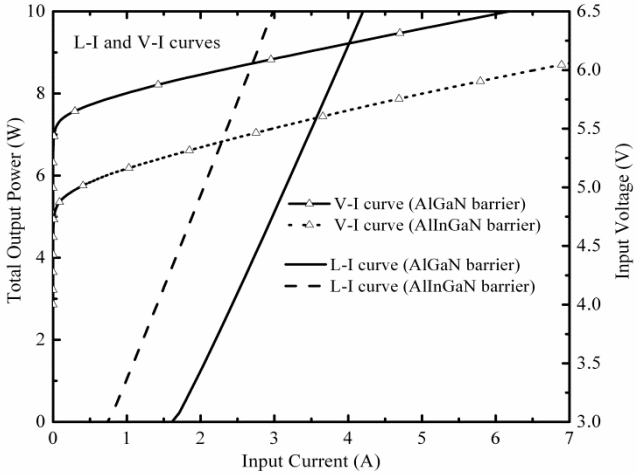

Figure 8. Comparison of L-I and V-I curves with ternary AlGaN and quaternary AlInGaN QWBs respectively. Polarization charge matched $Al_{0.794}In_{0.065}Ga_{0.141}N$ QWB reduces threshold current by 57%, and increases slope efficiency by 10%. Threshold voltage is also reduced by 13%.

Band diagrams (above lasing threshold) and carrier densities for both ternary AlGaN and quaternary AlInGaN QWB designs are provided in Figure 9, demonstrating the ability of the quaternary QWB design to realize a polarization-charge-minimized active region that improves the electroluminescence efficiency significantly.

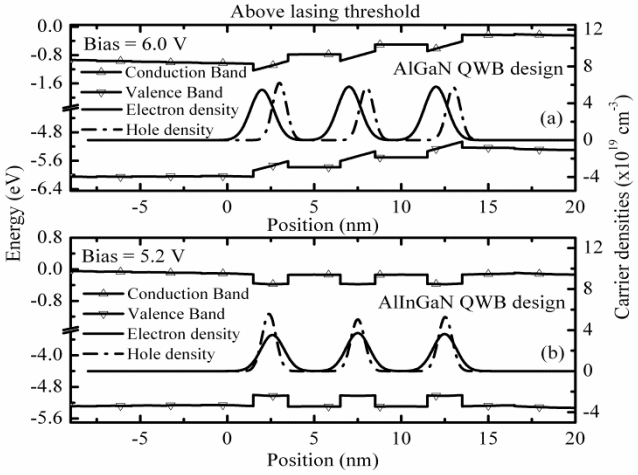

Figure 9. Energy band diagrams (above lasing threshold) and carrier densities of ternary AlGaN (a) and quaternary AlInGaN (b) QWB design. Polarization charge induced built-in electric field is completely eliminated in (b). This reduces threshold voltage and improves electroluminescence efficiency significantly.

Through careful design, further optimization of this structure is possible. Using ternary QWBs, we determined that it is not possible to use QWs thicker than 2.0 nm to increase optical confinement factor [4, 5], as thicker QWs would lead to unacceptably high spatial separation of the quasi-bound electron and hole populations [4, 6]. With polarization charge matched quaternary QWBs, however, QW thicknesses can be increased beyond 2.0 nm. We have investigated LD performance for different QW thicknesses. Thicker QW designs exhibit lower threshold current, primarily due to a larger optical confinement factor. It should be mentioned that change in QW thickness also influences lasing wavelength. A small red-shift is observed in thicker QW designs (see Figure 10). The red-shift can be explained from the perspective of a simple one-dimensional (1-D) rectangular potential well problem. In a 1-D rectangular well, the quantized ground state energy level comes closer to the bottom of the well as the well is made thicker. Hence, the lasing transition energy between electron and hole ground states becomes slightly smaller. Although optical confinement factor shows an approximately linear relationship with QW thickness, non-uniform distribution of carriers among QWs may become significant if QW thickness is increased arbitrarily, and ultimately degrade electroluminescence efficiency. Figure 11 shows that the threshold current of our quaternary QWB design may be approximately minimized with a QW thickness of 3.5 nm. For QWs thicker than 4.0 nm, lack of homogeneity of carrier distribution among the QWs begins to outweigh the advantage of enhanced optical confinement factor. This is why there is a minimum on threshold current vs. QW thickness plot (see Figure 11). With larger net interfacial polarization charge, this minimum may occur at a smaller thickness [7].

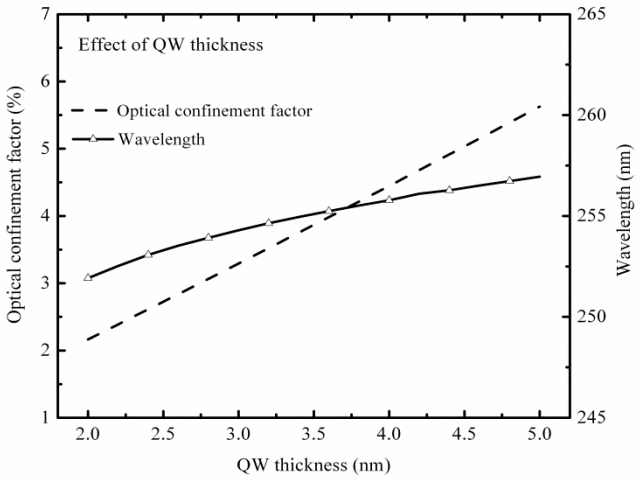

Figure 10. Effect of QW thickness on optical confinement factor and lasing wavelength. In a thicker rectangular potential well, quantized ground energy level comes closer to the bottom of the well. This explains why lasing wavelength becomes slightly longer in thicker QW design.

So far, we have investigated designs with $Al_{0.794}In_{0.065}Ga_{0.141}N$ as the QWB, though many other polarization-minimizing choices for quaternary material compositions are possible. It is possible, for example, to choose polarization matched quaternaries with different bandgap energy. Figure 12 shows how bandgap energy (bulk and unstrained) varies along the locus of

polarization charge minimized quaternaries. With a different quaternary QWB, we can modify QW depths in the conduction band and the valence band. LD designs with shallow QWs will yield higher threshold current because only a small fraction of injected carriers will be captured inside the QWs. On the other hand, the distribution of carriers will be non-uniform if QWs are very deep [8], and one must anticipate variation of lasing wavelength with QWB bandgap energy. Figure 13 compares the L-I curves of three different QWB designs. Low threshold current is observed with larger band offsets. Unfortunately, there is an upper limit of band offsets that cannot be exceeded in our design. The maximum bandgap offset, ΔE_g that can be achieved in our polarization charge minimized design with $Al_{0.535}Ga_{0.465}N$ QWs is 0.75 eV (see Figure 12). However, longer UV wavelength designs can surely take advantage of comparatively deeper QWs to capture a large fraction of injected carriers. Typically, band offset ratio (ΔE_c:ΔE_v) is 50:50 [9] or 70:30 [10] for AlGaN/GaN material interfaces. But, it is possible to have different ratios if material interface involves AlInGaN quaternary compositions. Electron affinity of InN is significantly larger than that of AlN [11]. Hence, it is possible to make ΔE_c significantly smaller than ΔE_v (and vice-versa) if quaternary mole composition is chosen appropriately. Such an interface may not have minimized polarization charge.

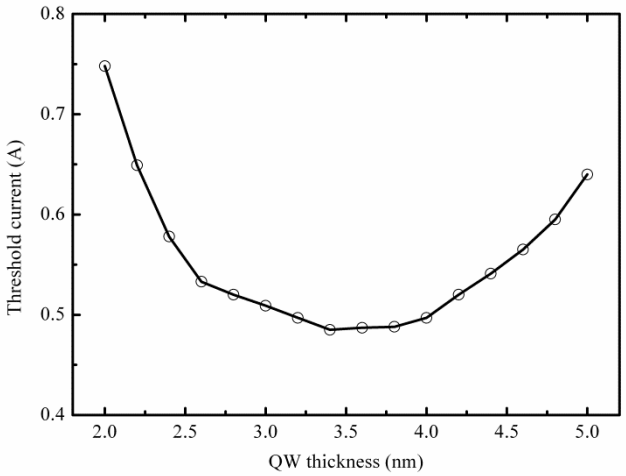

Figure 11. Effect of QW thickness on threshold current. Thinner (< 2.5 nm) QW designs suffer from reduced optical confinement factor. On the other hand, thicker (> 4.0 nm) QW designs give rise to non-uniformity among QWs carrier populations, which reduces electroluminescence efficiency and increases threshold current in spite of very large optical confinement factor.

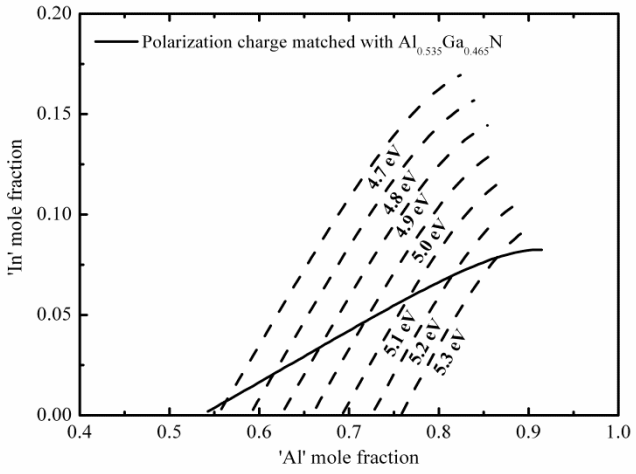

Figure 12. Locus of polarization charge minimized quaternary AlInGaN compositions together with contours of constant bandgap energy (bulk and unstrained).

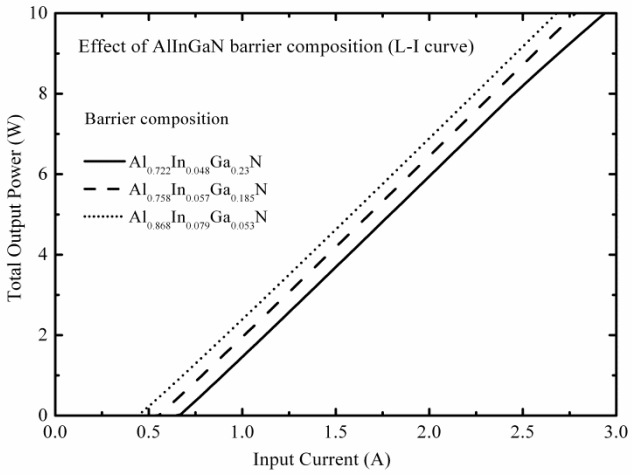

Figure 13. Comparison of L-I curves with different quaternary QWBs. For these simulations, 3.5 nm thick QWs have been assumed.

Our ability to grow a polarization charge minimized (or free) active region depends on how precisely we can control the mole composition of AlInGaN quaternaries. It has been reported that growth of high crystalline quality AlInGaN layers is difficult [12], though such issues do not appear to be fundamental. Recently, Sakalauskas *et al.* have grown a wide range of AlInGaN materials on c-place sapphire substrates with GaN templates [13] and studied their optical properties. They confirmed pseudomorphic growth of AlInGaN films by high-resolution x-ray diffraction measurements. Experimental studies like this inspire confidence in the prospect of realizing AlGaN-Based MQW DUV LDs on AlN substrates using polarization charge matched

AlInGaN QWBs. Yet, it may be challenging to control individual mole fractions with three digits of precision (± 0.001). Any deviation from the target quaternary QWB composition will increase net interface polarization charge. Nevertheless, significant improvement in device performance do not rely on the complete absence of interfacial polarization charge. In order to investigate the effect of partial polarization charge matching, we have simulated the LD structure of Table 2 with different magnitudes of net interfacial polarization charge in the active region. From the observed relationship between threshold current vs. net polarization charge, further reduction of threshold current becomes negligible for net polarization charge less than 0.0008 Cm^{-2} (results not shown here). Based on this study, we conclude that maintaining the magnitude of net polarization charge below 0.0008 Cm^{-2} is sufficient to effectively suppress any electron and hole wave function separation within the QWs. It is interesting to determine how far one can deviate from target quaternary mole compositions and remain within the tolerable limits of net interface polarization charge (< 0.0008 Cm^{-2}). For example, let us assume that our target mole composition is $Al_{0.794}In_{0.065}Ga_{0.141}N$. Figure 14 shows the contour line of quaternaries which will yield a net interface polarization charge (magnitude) of 0.0008 Cm^{-2} with $Al_{0.535}Ga_{0.465}N$ QWs. Any composition outside of the contour lines will yield higher polarization charge. For the 'Al' mole fraction, the error margin is ± 0.008 and that of indium (In) mole fraction is ± 0.002. It is important to note that even a partially minimized polarization charge (< 0.0112 Cm^{-2}) design will perform better than that of the structure with no charge matching.

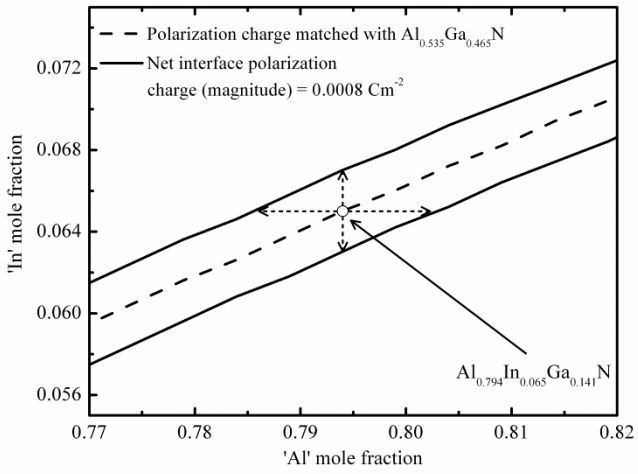

Figure 14. Contour of quaternaries with finite (0.0008 Cm^{-2}) net interface polarization charge together with the locus of polarization charge minimized quaternaries. Any quaternary composition inside the solid lines, will produce smaller net interface polarization charge (< 0.0008 Cm^{-2}) with $Al_{0.535}Ga_{0.465}N$.

Until now, we have explored designs with quaternary AlInGaN QWBs and ternary AlGaN QWs. Unfortunately, it is not possible to do it the other way around, i.e. with ternary QWBs and quaternary QWs. All the quaternary compositions that are polarization charge matched to a particular ternary AlGaN, have bandgap energies greater than that of the AlGaN ternary (see Figure 12), and provide no electrical confinement. It may be possible to design polarization charge free active regions using quaternaries for both QWBs and QWs [14], yet this approach

poses greater challenges for crystal growth.

III-N based lateral current injection DUV LD design:

As alluded to previously, one of the most significant side-effects of inefficient *p*-type doping of wide bandgap III-Nitride ternary material is the emergence of an unintentional "hole blocking layer" between the homogeneous quasi-neutral *p*-type material and the device active region, effectively preventing efficient hole injection. To circumvent all issues surrounding vertical injection designs in the DUV emission range, we have proposed a lateral current injection (LCI) LD design exploiting polarization- matched quaternary QWBs and regrown Ohmic contacts [15]. We have further demonstrated that such LCI LD designs significantly decouple the problem of electrical injection from that of optical confinement. Indeed, we propose the use of purely intrinsic wide-bandgap material for the optical waveguide layers of LCI LD designs for improved optical confinement. Our numerical simulations have demonstrated that regrown Ohmic result in no artificial blocking layers for lateral charge injection, but additionally serve to inhibit leakage of carriers from the active region and loss of quantum efficiency. Although the LCI LD design has already been proposed in the literature to be used as longer wavelength active sources in optoelectronic integrated circuits using GaInAsP/InP and related material systems, we presented the first theoretical demonstration [15] that this approach is also feasible for UV LDs operating at sub-300 nm wavelengths in the III-V nitride material system.

Table 3 shows the epitaxial structure of a 290 nm edge-emitting LCI LD design using polarization-charge-matched quaternary QWBs and regrown Ohmic contacts. It is assumed that all layers are pseudomorphically grown on top of an AlN substrate. Excellent optical confinement (15%) is predicted by two-dimensional calculations for 500 μm edge-emitting LD stripes formed by etching to a depth of 210 nm, or 150 nm above the top surface of the spacer. Ridge width is 2 μm and cavity length is 500 μm. Left and right facet reflectivities are assumed to be 85% and 95% respectively. Though we considered ten optical modes (TE) in all simulations, only one mode (the first order mode instead of the fundamental mode) participated in lasing over the range of injection currents considered. The corresponding optical mode profile is shown in Figure 15. Figure 16 illustrates the energy band diagrams and carrier densities at equilibrium as well as at a bias condition above the lasing threshold. L-I and V-I curves are shown in Figure 17.

Table 3: Epitaxial layer structure for an AlGaN/AlInGaN edge emitting LCI LD design operating at 290 nm. Both P- and N-waveguiding layer compositions are graded to redistribute interfacial polarization charge over their entire thickness.

Layer Name	Material	Thickness (nm)	Refractive index
P-waveguiding	AlN	210	2.15
Grading	$Al_{0.79}In_{0.11}GaN$~AlN	150	2.2475 ~ 2.15
Spacer	$Al_{0.79}In_{0.11}GaN$	5.0	2.2475
QW (×20)	$Al_{0.30}GaN$	2.0	2.255
QWB (×20)	$Al_{0.79}In_{0.11}GaN$	5.0	2.2475
Grading	AlN~$Al_{0.79}In_{0.11}GaN$	150	2.15 ~ 2.2475
N-waveguiding	AlN	2000	2.15
Substrate	AlN	-	2.15

Nickel and aluminum are considered as the p- and n-Ohmic metals, respectively. At 290 nm

wavelength, the absorption coefficient of nickel is 8.77×10^{5} cm^{-1} and that of aluminum is 1.49×10^{6} cm^{-1} [16]. Total optical loss in metals for the lasing mode of Figure 15 is 0.014 cm^{-1}. Higher order modes have considerably greater optical loss (> 8 cm^{-1}). Ternary AlGaN with 55% Al or more is assumed optically non-absorbing at λ = 290 nm and no other background optical loss is considered in our simulations. To estimate the absorption coefficient of AlGaN, a composition, strain and wavelength dependent complex refractive index model is used [17, 18]. But, the parameters used in the model are extracted from un-doped bulk samples. So, Mg doped p-type AlGaN may exhibit sub-bandgap absorption. At this moment, there is no model to quantify this absorption coefficient at the wavelength of our interest but this can be qualitatively incorporated in all simulation results with the introduction of phenomenological distributed optical loss.

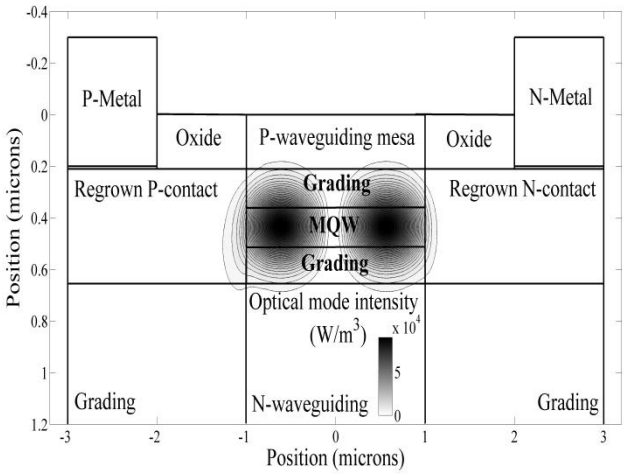

Figure 15. Optical mode profile corresponding to the epitaxial structure of Table 3 (Only the lasing TE mode is shown here). Insufficient lateral refractive index contrast between regrown contacts and MQW active region fails to confine higher order modes within the ridge width (results not shown here).

The entire epitaxial structure, with the exception of the regrown contacts, is assumed undoped to ensure that current flows laterally through the narrow bandgap QWs only. Besides, undoped epitaxial structure may offer reduced defect density which will increase Shockley–Read–Hall lifetimes and lower Auger recombination coefficients, improving both threshold current and quantum efficiency. The bandgap of the regrown Ohmic contacts should be sufficiently larger than that of the QWs to block the leakage of carriers from the active region, as well as assist in lateral optical confinement through their lower refractive index. The substitutional dopant (Si) concentration of the $Al_{0.60}GaN$ regrown n-contact was taken to be 2×10^{18} cm^{-3}. The valence band discontinuity, ΔE_v at the regrown n-contact/QW interface is 340 meV. Choosing appropriate and optimized material composition for the regrown p-contact is vital for LCI LD designs in the III-V nitride material system. To achieve lasing at 290 nm, it must have an Al mole fraction greater than 30% to block the leakage of electrons from the active region. Further increasing the Al composition, the conduction band discontinuity will increase (which is necessary to block electrons) but the p-type conductivity will degrade because of

higher Mg activation energy. With decreasing Al mole fraction, the exact opposite happens. Electrons leak from the active region and reach the regrown p-contact, where they recombine non-radiatively. Moreover, the optical mode(s) may shift towards the regrown p-contacts. In the present design, $Al_{0.55}GaN$ was determined to be the optimal material choice for the regrown p-contact, and a substitutional dopant (Mg) concentration of 3×10^{19} cm^{-3} has been assumed. The conduction band discontinuity, ΔE_c at the regrown p-contact/QW interface is 371 meV.

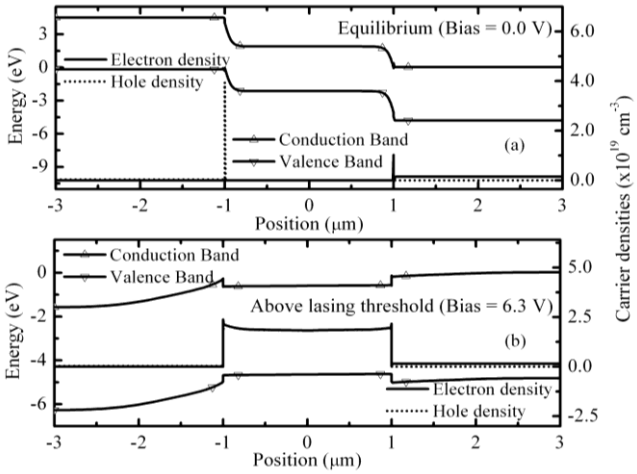

Figure 16. Energy band diagrams and carrier densities (a) at equilibrium and (b) above the lasing threshold.

Grading is applied at the bottom of the regrown contacts to redistribute polarization charge volumetrically and to prevent the formation of a parasitic lateral current leakage path. Similarly, grading is used on top of the N-waveguiding layer and below the P-waveguiding layer to eliminate parasitic channels and to ensure uniform distribution of carriers from the top QW to the bottom one. $Al_{0.79}In_{0.11}GaN$ (used for the QWB) has the largest bandgap and it is polarization charge matched to $Al_{0.30}GaN$ (used for the QW). Polarization charge matching both reinforces uniform carrier distribution vertically among the QWs, and reduces electron and hole wavefunction separation. The wide bandgap of the QWBs ensures that current flows laterally through the QWs only. Because of this and minimized non-radiative recombination rates at the regrown contacts, injection efficiency is expected to be high. One particular advantage of the LCI LD design over vertical injection designs is that they can support a larger number of QWs [19-21] without introducing significant nonuniformity in the carrier distribution among the wells. However, in a design employing too many QWs, the total thickness of an active region grown on top of an N-waveguiding layer may exceed the critical thickness for pseudomorphic growth, and those QWs at the top of the structure may suffer from reduced TE optical gain due to lack of compressive strain [1]. On the other hand, the threshold current density will be higher in LCI LD designs using only a few QWs. Regardless of the number of QWs, the lateral carrier distribution inside the wells may become nonuniform above lasing threshold (see Figure 16). This can be attributed to the disparity of electron and hole mobilities [22]. Above the lasing threshold it is observed that carrier densities exhibit a lateral peak at the interfaces with regrown Ohmic contacts [19] (see Figure 16). Like the lasing mode of Figure 15, the stimulated emission profile

(not shown here) also peaks close to these interfaces, with reduced emission in the middle of the active region [22]. This is why the 1st order mode (total two lobes and both of them inside the active region) lased instead of the fundamental mode because the 1st order mode is pumped more efficiently.

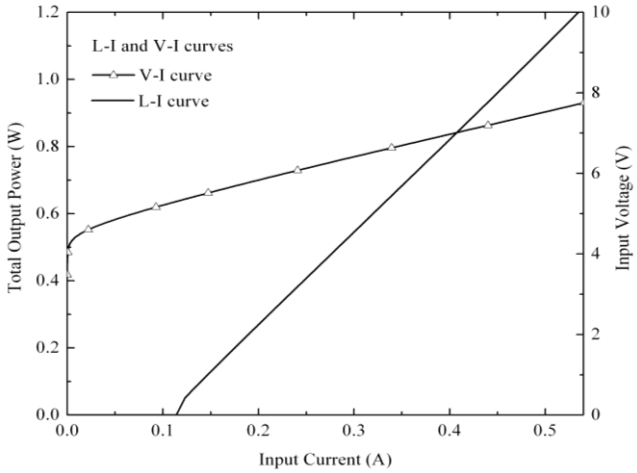

Figure 17. L-I curve and V-I curve of the epitaxial structure of Table 3.

The threshold current density of the proposed design is calculated to be 157 kA/cm^2. To estimate this threshold current density, the lateral cross-section of the entire MQW stack has been considered. In the literature, a cross-sectional area of ridge width and cavity length is used to normalize threshold current [23] which is not correct for LCI type LDs [24]. A simple prescription for decreasing threshold current density in LCI designs is to use thicker QWBs. However, care must be taken to ensure that the optical confinement factor is not degraded by a large margin, and the critical thickness for pseudomorphic growth is not exceeded by the active region. Thicker QW designs demand more threshold current for population inversion. During lasing more voltage is dropped laterally across the regrown p-contact than any other region because of its moderate p-type conductivity. This in turn may reduce the effectiveness of the conduction band offset to block electrons. Also, the lasing wavelength increases with the thickness of QWs.

One major disadvantage of the LCI LD design is that a large current must flow through a small lateral cross-section of the active region. In a vertical injection design, current flows instead through the larger cross-sectional area of the mesa. However, with the help of a large number of QWs, Joule heating (P_{heat}) may be distributed over a larger volume in an LCI design, reducing the average temperature. The temperature difference between the active region and the heat sink can be estimated with the expression $\Delta T = R_{th} \times P_{heat}$ where R_{th} is the thermal resistance [18]. At an injection current level of 150 mA, ΔT is approximately 52 K assuming that R_{th} = 75 K/W. Based on this rough estimate, it can be concluded that the design presented in Table 3 may be operated in CW mode instead of pulse mode.

AlGaN based DUV Laser diode using inverse-tapered P-waveguide:

Recently, we have demonstrated that the hole injection efficiency of vertical injection AlGaN DUV LDs can be improved significantly by employing an inverse tapered *p*-waveguiding layer

instead of the conventionally tapered EBL. Numerical simulation revealed that along the c-axis, inverse tapered *p*-type AlGaN layer offers a flat and smooth valence band, a pre-requisite for efficient hole injection into the MQW active region. Furthermore, we have proposed a transparent narrow-bandgap *n*-waveguiding layer to pull the optical mode away from the highly absorptive *p*-Ohmic metal. A manuscript is written recently (awaiting submission) to demonstrate a ternary AlGaN 290 nm vertical injection LD design featuring inverse tapering. The inverse tapering efficacy can be easily extended to shorter wavelengths (~ 250 nm).

To achieve superior hole injection efficiency and minimum optical loss in the p-Ohmic metal, we have explored different p-waveguide layer and EBL designs by means of numerical simulation. Table 4 lists the epitaxial layer structure of a typical AlGaN/AlGaN edge emitting vertical injection LD design with a conventionally tapered EBL. It is assumed that all layers are pseudomorphically grown [1, 3] on top of an AlN substrate. 500 μm edge emitting LD stripes are formed by etching to a depth of 310 nm, or 220 nm above the top surface of the spacer, with lasing at λ = 290 nm. The ridge width is 2 μm and cavity length is 500 μm. Left and right facet reflectivities are assumed to be 85% and 95% respectively (Mirror loss is 2.14 cm^{-1}). We have considered several TE and TM modes in all simulations, and confirmed that only the fundamental modes are strongly confined by the optical waveguide. Of the two fundamental modes, lasing occurs only in the TE mode over the range of injection currents we have studied, as is expected in compressively strained AlGaN based MQW LD designs [1, 3]. Its optical mode profile is shown in Figure 18. Refractive indices used for optical mode calculations are presented in Table 4, and are estimated from the real part of a complex refractive index model [11, 18].
Optical loss in metals plays a critical role in determining the threshold current. For purposes of our numerical calculation, the p- and n-Ohmic metals are taken to be nickel and aluminum, respectively. At λ = 290 nm, the total optical loss is 2.4 cm^{-1} in the metals for the lasing mode of Figure 18. Figure 19 illustrates the energy band diagram at a bias condition below the lasing threshold. L-I and V-I curves are shown in Figure 20. The threshold current is 715 mA and the slope efficiency is 0.08 W/A.

Table 4: Epitaxial layer structure for an AlGaN/AlGaN edge emitting vertical injection LD design operating at 290 nm.

Layer Name	Material	Thickness (nm)	Refractive index
Contact	GaN	10	2.603
p-waveguide	$Al_{0.48}GaN$	500	2.624
EBL	$Al_{0.54\sim0.60}GaN$	20	2.565 ~ 2.522
Spacer	$Al_{0.54}GaN$	5.0	2.565
QW (×2)	$Al_{0.34}GaN$	2.0	2.741
QWB (×2)	$Al_{0.54}GaN$	5.0	2.565
Grading	$Al_{0.45\sim0.54}GaN$	20	2.662 ~ 2.565
n-waveguide	$Al_{0.45}GaN$	150	2.662
Grading	$Al_{0.70\sim0.45}GaN$	400	2.46 ~ 2.662
Buffer	$Al_{1.00\sim0.70}GaN$	1000	2.292 ~ 2.46
Substrate	AlN	-	2.292

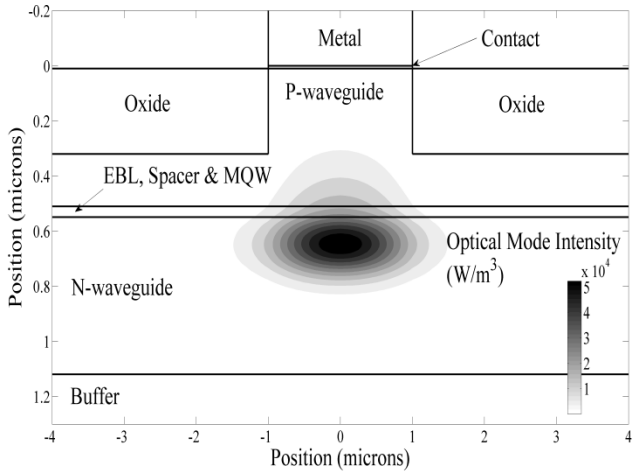

Figure 18. Optical mode profile corresponding to the epitaxial structure of Table 4 (Only the lasing TE mode is shown here).

In contrast to previously reported designs [1, 3], the epitaxial layer structure of Table 4 exhibits several new features. It only employs ternary AlGaN compositions and avoids ternary AlInN and quaternary AlInGaN. Although AlInN and AlInGaN based designs may offer promising LD performance advantages [1, 3], high quality crystal growth of In-rich materials is presently considered more challenging. In order to achieve higher p-type conductivity, narrow bandgap $Al_{0.48}GaN$ (E_{gap} = 4.58 eV) is utilized for the p-waveguide layer. Wider bandgap material would incur greater Joule heating because of poor p-type conductivity. On the other hand, narrow bandgap p-waveguide material may become optically absorptive at the lasing wavelength, and will moreover exacerbate optical losses by pulling the optical mode towards the highly absorptive p-Ohmic metal. Similarly, a thinner p-waveguide layer would yield higher optical loss, while a thicker layer would introduce additional series resistance and associated Joule heating. In contrast to previously reported designs [1, 3], the optical mode profile of devices presented in this article is no longer centered on the active region (See Figure 18). A narrow bandgap n-waveguide layer is employed to counterbalance the high refractive index of the proposed p-waveguide layer, and to pull the optical mode downwards, away from the lossy p-Ohmic metal. The optical confinement factor is 0.75 %. Thicker and narrower bandgap n-waveguide material may reduce lateral series resistance (and Joule heating) but it would significantly degrade the optical confinement factor and may also introduce additional optical absorption. Furthermore, a thinner and/or wider bandgap AlGaN n-waveguide layer may not be able to pull the optical mode downwards effectively.

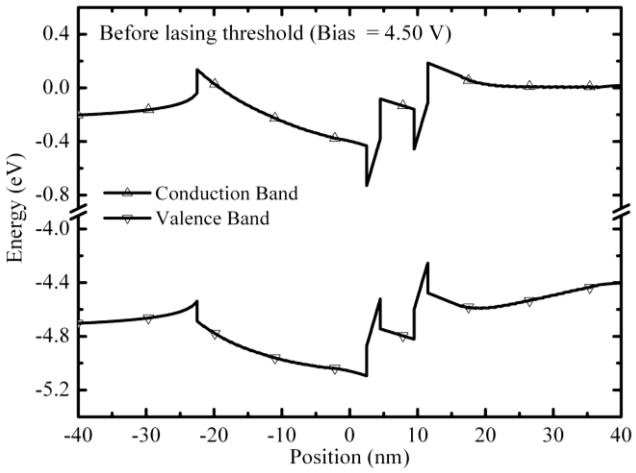

Figure 19. Energy band diagram of the epitaxial structure of Table 4 at a bias before the lasing threshold. Conventionally tapered EBL is also acting as a significant hole blocking layer.

From the energy band diagram of Figure 19, one may observe that a conventionally tapered EBL (in which the bandgap increases along the growth direction) acts as a large hole blocking layer primarily due to the unscreened polarization charge at the p-waveguide layer/EBL and spacer/QW interfaces. The substitutional dopant (Mg) concentration of the spacer, EBL and p-waveguide layer is taken to be 10^{18} cm^{-3} (For the n-waveguide layer, the substitutional Si concentration is assumed to be 2×10^{18} cm^{-3}). We point out that the prominence of this hole blocking layer will be artificially but only partially masked if 100% ionization of dopant atoms is assumed; however, this is not only incorrect, but also leads to a gross overestimate of hole injection efficiency.

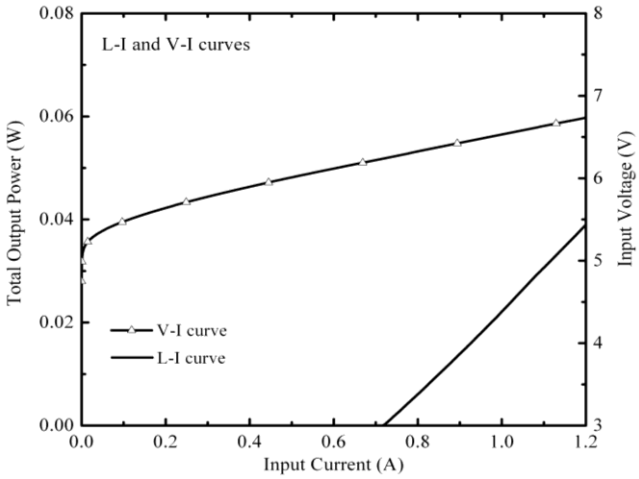

Figure 20. L-I and V-I curve of the epitaxial structure of Table 4.

One way to reduce the potential barrier for hole injection is to dope the p-type layers heavily. Figure 21 shows the effect of heavy Mg doping on the energy band diagram. As expected, the barrier height of the hole blocking layer is reduced significantly. Both threshold current and voltage are lowered due to improved hole injection efficiency (see Figure 22). Although heavy doping degrades carrier mobility [25-27], this effect alone does not exert a large influence on either threshold current or voltage. Instead, it is the energetic barrier to hole injection due to the valence band discontinuity at the p-waveguide layer/EBL interface with conventional tapering which is the dominant effect, limiting the mechanism for hole injection to mere thermionic emission.

The abrupt valence band discontinuity at the p-waveguide layer/EBL interface can be eliminated by using an EBL with two step tapering. Specifically, the bottom half of the EBL may be tapered upwards such that its bandgap increases in the growth direction (from $Al_{0.54}GaN$ to $Al_{0.60}GaN$) for efficient electron blocking. The upper half may be tapered downwards along the direction of growth (from $Al_{0.60}GaN$ to $Al_{0.48}GaN$) to eliminate abrupt valence band discontinuities. We have simulated the baseline epitaxial structure of Table 4 by replacing the conventionally tapered EBL with the proposed two step tapered design, and the results are shown in Figures 23 and 24. For meaningful comparison, the EBL thickness is held constant at 20 nm. Two step tapering of the EBL yields a 46% reduction in threshold current and 76% improvement in slope efficiency (see Figure 24). Unfortunately, the band diagram of Figure 23 clearly indicates that the two step tapered EBL does not reduce the size of the potential barrier to hole injection, but merely halves its effective thickness and eliminates the abrupt valence band offset. To improve the hole injection efficiency further, it is important to investigate and understand the nature of this polarization charge induced hole blocking layer in more detail.

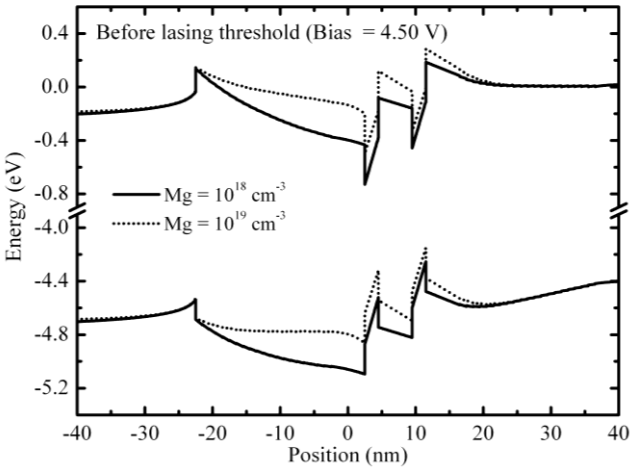

Figure 21. Effect of heavy Mg doping on the energy band diagram of the epitaxial structure of Table 4. Hole blocking layer is suppressed significantly.

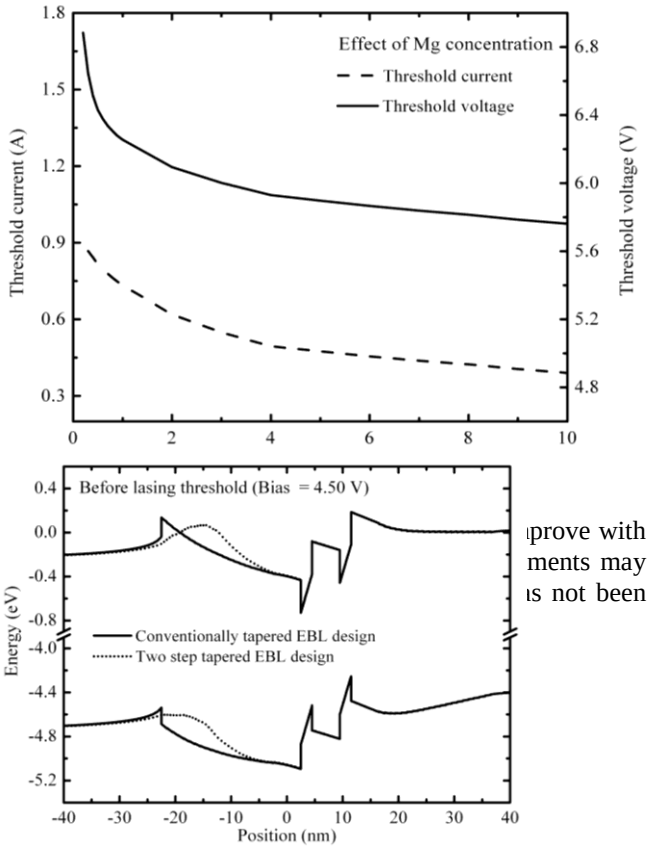

Figure 23. Comparison of the energy band diagrams between conventionally tapered and two step tapered EBL designs. Two step tapering eliminates the abrupt valence band offset at the P-waveguiding layer/EBL interface and reduces the effective thickness of the hole blocking layer.

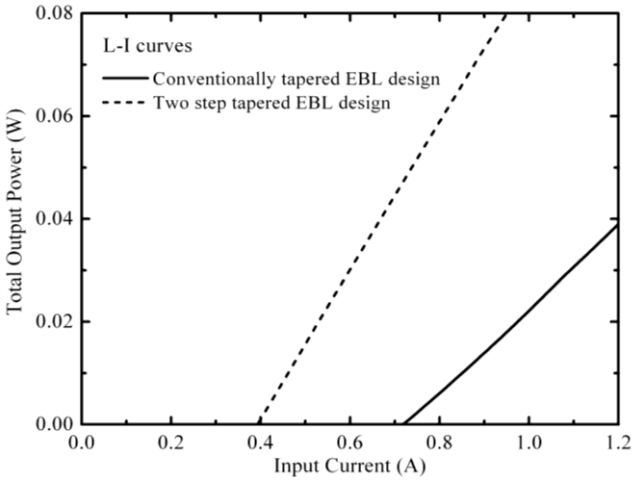

Figure 24. Comparison of L-I curves between conventionally tapered and two step tapered EBL designs. With two step tapering, threshold current is reduced by 46% and slope efficiency is improved by 76%.

The sign and magnitude of the net interface polarization charge of an $Al_xGa_{1-x}N/Al_yGa_{1-y}N$ interface depends on several factors, including growth axis, metal-face vs. N-face growth, difference between mole fraction x and y and their relative significance [11]. In our simulation, metal-face c-axis growth is assumed. It is obvious that a large mole fraction contrast will increase the magnitude of the net interface charge, but it is the sign of the difference between x and y which determines the sign of the polarization charge. If we assume that a layer of $Al_xGa_{1-x}N$ is grown on top of $Al_yGa_{1-y}N$, the net interface polarization charge will be positive if $x > y$ and vice versa (see Figure 25). Therefore, the volumetrically redistributed polarization charge of the two step tapered EBL is positive in the bottom half and negative in the upper half. With moderate dopant (Mg) concentration in the p-type layers (10^{18} cm^{-3}), this redistributed polarization charge opposes the bound charges associated with dopant atoms at the bottom half of EBL and reinforces at the top. In cases where the magnitude of the redistributed polarization charge in the lower half of the EBL exceeds the charge of electrically active dopant atoms in that layer, the location of the p-n junction itself is transferred to the interface between the two halves of the EBL. This explains why the effective thickness of the hole blocking layer is halved in a two-step tapered EBL design. Because the volumetric redistribution of polarization charge in the upper half contributes additively to the fixed charge contributed by ionized Mg atoms, the potential drop over the EBL layer is primarily across the bottom half, while the valence band is almost flat throughout the upper half (see Figure 23).

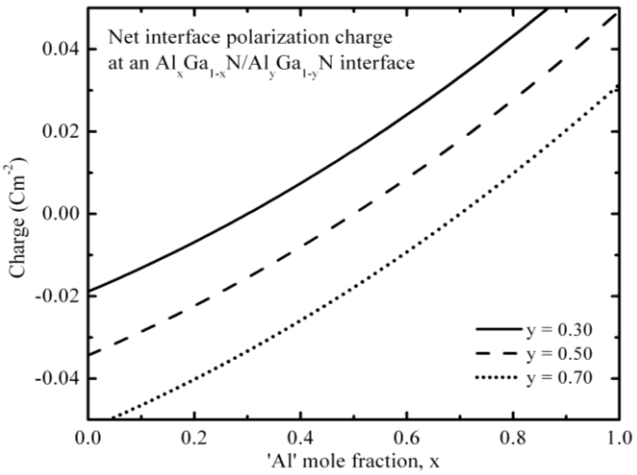

Figure 25. Compositional dependence of the net interface polarization charge at an AlGaN/AlGaN interface. It is assumed that the layers are pseudomorphically grown on top of AlN substrate.

Now that the root cause of the hole blocking layer has been identified, the next step is to address strategies for its suppression. One such approach is to flip the sign of the polarization charge at the bottom half of two step tapered EBL, in such a way that the redistributed polarization charge should be negative throughout the entire thickness of the EBL. From a compositional perspective, this means that the two step tapered EBL should be replaced by an inverse tapered p-waveguide layer where the bandgap should decrease along the growth direction. This may be a risky proposition, as electrons may leak from the MQW active region in the absence of an explicit EBL, and thereby degrade LD performance. However, in spite of the band diagram under flatband conditions, our numerical simulations reveal that above the lasing threshold, neither the conventional nor the two step tapered EBL are effective in blocking electrons anyway, due to the redistribution of electrostatic potential under strong forward bias. Indeed, because of poor p-type conductivity, a large fraction of the applied voltage is dropped across the EBL. This point is demonstrated in Figure 26. Above the lasing threshold, the conduction band is almost flat at the bottom half of the two step tapered EBL, and the only thing impeding the leakage of electrons is the conduction band offset at the spacer/QW interface. Nevertheless, in spite of electron leakage, this device can be made to lase, albeit at high injection current density. A similar result is observed for the conventionally tapered EBL (results not shown here). This observation suggests that the inverse tapering efficacy in DUV LD design may actually solve the problem of poor hole injection. Still, care must be taken to keep the electron leakage within tolerable limits via appropriate selection of MQW (and spacer) material compositions.

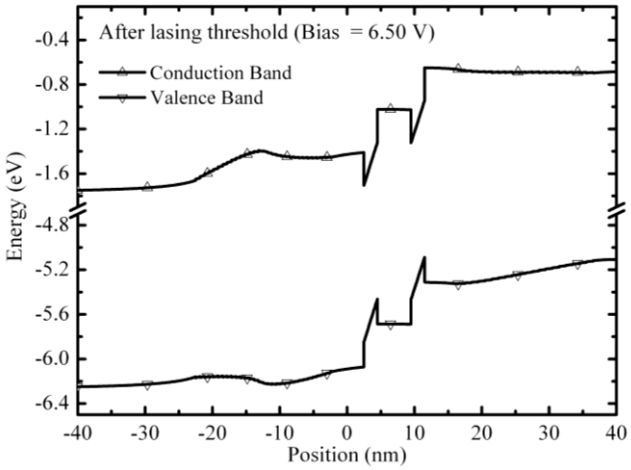

Figure 26. Energy band diagram of the two step tapered EBL design above lasing threshold. A large fraction of the applied voltage drops across the EBL and makes the conduction band almost flat.

We therefore modify baseline design of Table 4 by replacing the tapered EBL with an inverse tapered p-waveguide layer (from $Al_{0.54}GaN$ to $Al_{0.48}GaN$). Inverse tapering is affected over a thickness of 20 nm, with all other quantities unchanged. Simulation results show that the parasitic electrostatic barrier to hole injection is suppressed significantly (see Figure 27). Excellent hole injection efficiency leads to the dramatic improvement in LD performance shown in Figure 28. The L-I characteristic of two step tapered EBL design is included for comparison. The proposed inverse tapered design's threshold current is reduced by 33% and slope efficiency is improved by 14% with respect to the two step tapered EBL design. Threshold voltage is also reduced by 0.4 V (results not shown here). As there is no explicit EBL in the inverse tapered design, leakage of electrons from the active region can only be kept within acceptable limits if MQW and spacer compositions are chosen judiciously. To investigate this, we have studied the influence of different spacer compositions on the inverse-tapered design described. The material composition of the QWBs are kept identical to that of the spacer to ensure similar emission wavelength among the QWs. Figure 29 shows how the threshold current, lasing wavelength and optical confinement factor change with spacer (and QWB) composition. Rapid degradation of threshold current indicates that electron leakage becomes dominant if the aluminum content falls below 54%. 59% Al minimizes the threshold current (and electron leakage), incurring a small red-shift to the emission wavelength. The red-shift can be easily corrected by modifying QWs' composition and/or thickness. For aluminum content in excess of 60%, threshold current starts rising sharply because of degradation of optical confinement and further separation of electron and hole wavefunctions within the QWs.

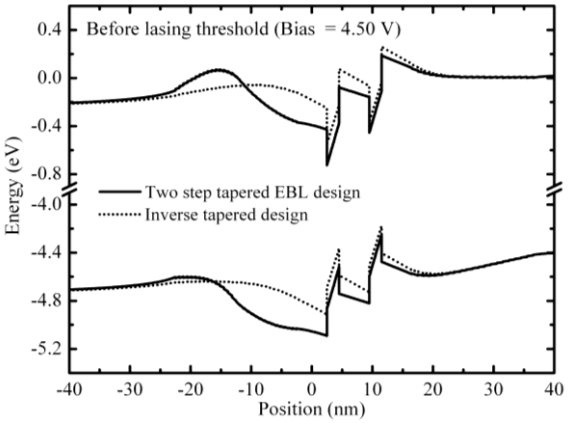

Figure 27. Comparison of the energy band diagrams between two step tapered EBL and inverse tapered designs. Inverse tapering reduces the potential barrier of the hole blocking layer by 180 meV.

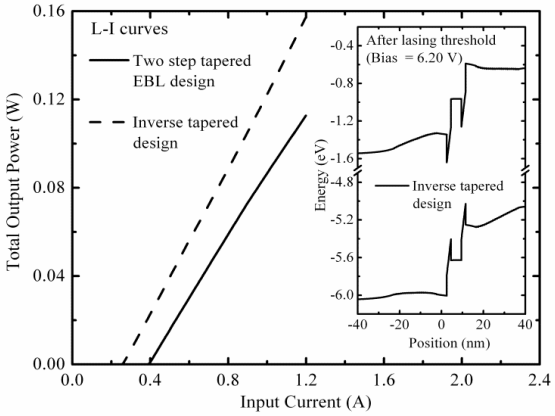

Figure 28. Comparison of L-I curves between two step tapered and inverse tapered designs. Inverse tapering reduces threshold current by 33% and improves slope efficiency by 14%. Inset shows the energy band diagram of the inverse tapered design above the lasing threshold, and the clear absence of potential barriers to hole injection.

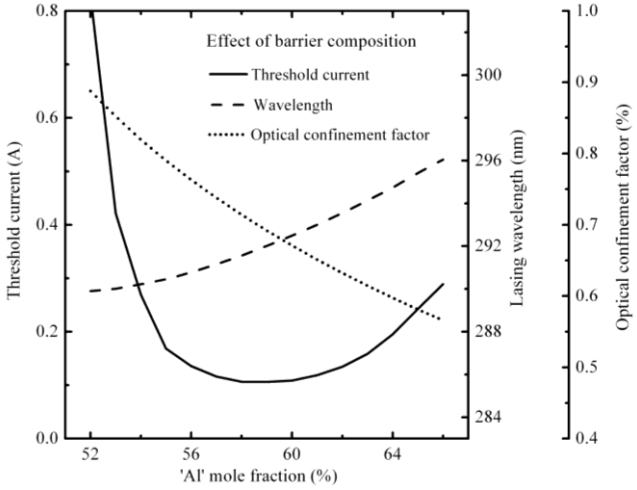

Figure 29. Effect of QWBs and spacer's composition on the threshold current, lasing wavelength and optical confinement factor. Narrow bandgap barriers fail to block electron leakage. On the contrary, wider bandgap QWBs (and spacer) pushes the optical mode downwards and red-shits emission wavelength via quantum-confined stark effect (QCSE).

Many researchers have proposed different approaches for improving the conductivity of p-type layers, hole injection efficiency and electrical confinement of carriers inside the active region in LDs and LEDs operating within the visible and UV spectrum. Several articles are cited in Satter *et al*. [3] which report new strategies for reduction of the high activation energy of Mg dopants or the increase of free hole concentration in III-N materials. A technique known as "polarization doping" has been suggested for the improvement of p-type dopant (Mg) ionization efficiency in compositionally graded AlGaN layers through the field ionization of the dopant atoms via the electric field induced by polarization charge [9, 28-33]. This appellation is somewhat misleading, as electric fields of sufficient magnitude to ionize deep acceptor atoms would necessarily drive free carriers away from the high-field region, leaving behind only fixed space charge rather than highly conductive material. Instead, compositional grading can volumetrically redistribute sufficient negative polarization charge to make it energetically favorable for free holes in adjacent material to drift or diffuse into the compositionally graded region, thereby creating a high free hole density irrespective of whether Mg atoms are electrically active. Both N-face [9, 28, 29, 32] and the conventional metal-face [30, 31, 33] growth can benefit from compositional grading, producing a flat and smooth valence band profile right up to the edge of the active region to ensure superlative hole injection efficiency. If N-face growth is adopted, one must not only ensure good crystalline quality of the epitaxial layers, but also make Ohmic contact to a wide bandgap p-type layer [31].

Several authors have reported SPSL based EBLs [34, 35] to improve hole injection efficiency and electrical confinement of electrons. Although this strategy effectively reduces hole blocking barrier height, it also directly introduces deep hole traps which impede the vertical transport of holes through these layers. Lattice matched ternary AlInN [36] and polarization charge matched

(partial) quaternary AlInGaN EBLs [37] have also been used to improve hole injection efficiency and electrical confinement of electrons. From the growth perspective, one of the most attractive features of our proposed inverse tapered design is that it is an all AlGaN based design and it does not critically depend on the polarization charge matching via precise control of quaternary compositions.

Task 3 Conclusions:

Our design efforts via numerical simulation have addressed some of the most critical problems that plague the III-N based electrical injection DUV laser designs. The final inverse-tapered design is definitely feasible with the current growth technology and is a very likely contender that may actually work and live up to its promises. Surely, the successful operation will critically depend on the material growth quality and the deviation of the actually grown epitaxial structure from the 'proposed structure'.

References for Task 3:

[1] M. M. Satter, H. J. Kim, Z. Lochner, J. H. Ryou, S. C. Shen, R. D. Dupuis, and P. D. Yoder, "Design and Analysis of 250-nm AlInN Laser Diodes on AlN Substrates Using Tapered Electron Blocking Layers," *IEEE Journal of Quantum Electronics,* vol. 48, pp. 703-711, May 2012.

[2] N. Khan, N. Nepal, A. Sedhain, J. Y. Lin, and H. X. Jiang, "Mg acceptor level in InN epilayers probed by photoluminescence," *Applied Physics Letters,* vol. 91, p. 012101, 2007.

[3] M. M. Satter, Z. Lochner, J. H. Ryou, S. C. Shen, R. D. Dupuis, and P. D. Yoder, "Polarization Matching in AlGaN-Based Multiple Quantum Well Deep Ultraviolet Laser Diodes on AlN Substrates using Quaternary AlInGaN Barriers," *Journal of Lightwave Technology,* vol. 30, pp. 3017-3025, 2012.

[4] A. Venkatachalam, B. Klein, J. H. Ryou, S. C. Shen, R. D. Dupuis, and P. D. Yoder, "Design Strategies for InGaN-Based Green Lasers," *Ieee Journal of Quantum Electronics,* vol. 46, pp. 238-245, Feb 2010.

[5] P. J. Parbrook and T. Wang, "Light Emitting and Laser Diodes in the Ultraviolet," *Ieee Journal of Selected Topics in Quantum Electronics,* vol. 17, pp. 1402-1411, Sep-Oct 2011.

[6] A. Venkatachalam, P. D. Yoder, B. Klein, and A. Kulkarni, "Nitride band-structure model in a quantum well laser simulator," *Optical and Quantum Electronics,* vol. 40, pp. 295-299, 2008.

[7] G. E. Dialynas, G. Deligeorgis, M. Zervos, and N. T. Pelekanos, "Influence of polarization field on the lasing properties of III-nitride quantum wells," *Physica E: Low-dimensional Systems and Nanostructures,* vol. 32, pp. 558-561, 2006.

[8] S. Mogg and J. Piprek, "Optimization of the barrier height in 1.3 mu m InGaAsP multiple-quantum-well active regions for high temperature operation," *Physics and Simulation of Optoelectronic Devices Ix,* vol. 4283, pp. 227-237, 2001.

[9] J. Piprek, "Ultra-violet light-emitting diodes with quasi acceptor-free AlGaN polarization doping," *Optical and Quantum Electronics,* vol. 44, pp. 67-73, 2011.

[10] S. H. Ha, S. L. Ban, and J. Zhu, "Intersubband absorption in strained AlGaN/GaN double quantum wells," *Physica B: Condensed Matter,* vol. 406, pp. 3640-3645, 2011.

[11] J. Piprek, *Nitride semiconductor devices : principles and simulation*. Weinheim: Wiley-VCH, 2007.

[12] H. J. Chung, R. J. Choi, M. H. Kim, J. W. Han, Y. M. Park, Y. S. Kim, H. S. Paek, C. S. Sone, Y. J. Park, J. K. Kim, and E. F. Schubert, "Improved performance of GaN-based blue light emitting diodes with InGaN/GaN multilayer barriers," *Applied Physics Letters,* vol. 95, p. 241109, 2009.

[13] E. Sakalauskas, B. Reuters, L. R. Khoshroo, H. Kalisch, M. Heuken, A. Vescan, M. Röppischer, C. Cobet, G. Gobsch, and R. Goldhahn, "Dielectric function and optical properties of quaternary AlInGaN alloys," *Journal of Applied Physics,* vol. 110, p. 013102, 2011.

[14] M. A. Caro, S. Schulz, S. B. Healy, and E. P. O'Reilly, "Built-in field control in alloyed c-plane III-N quantum dots and wells," *Journal of Applied Physics,* vol. 109, p. 084110, 2011.

[15] M. M. Satter, Z. Lochner, J.-H. Ryou, S.-C. Shen, R. D. Dupuis, and P. D. Yoder, "AlGaN-Based Lateral Current Injection Laser Diodes Using Regrown Ohmic Contacts," *IEEE Photonics Technology Letters,* vol. 25, pp. 313-316, 2013.

[16] M. Polyanskiy. (01/20/2013). *Refractive Index Database*. Available: http://refractiveindex.info

[17] J. Piprek, *Nitride semiconductor devices : principles and simulation*. Weinheim: Wiley-VCH ; [Chichester : John Wiley [distributor]], 2007.

[18] J. Piprek, *Semiconductor optoelectronic devices : introduction to physics and simulation*. Amsterdam ; Boston: Academic Press, 2003.

[19] N. N. Akram, "Lateral current injection (LCI) multiple quantum-well 1.55 mu m laser with improved gain uniformity across the active region," *Optical and Quantum Electronics,* vol. 36, pp. 827-846, Jul 2004.

[20] D. A. Suda, H. Lu, T. Makino, and J. M. Xu, "An Investigation of Lateral Current Injection-Laser Internal Operation Mechanisms," *Ieee Photonics Technology Letters,* vol. 7, pp. 1122-1124, Oct 1995.

[21] E. H. Sargent, D. A. Suda, A. Margittai, F. R. Shepherd, M. Cleroux, G. Knight, N. Puetz, T. Makino, A. J. SpringThorpe, G. Chik, and J. M. Xu, "Experimental study of LCI lasers fabricated by single MOCVD overgrowth followed by selective dopant diffusion," *Ieee Photonics Technology Letters,* vol. 10, pp. 1536-1538, Nov 1998.

[22] T. Okumura, M. Kurokawa, M. Shirao, D. Kondo, H. Ito, N. Nishiyama, T. Maruyama, and S. Arai, "Lateral current injection GaInAsP/InP laser on semi-insulating substrate for membrane-based photonic circuits," *Optics Express,* vol. 17, pp. 12564-12570, Jul 20 2009.

[23] T. Okumura, H. Ito, D. Kondo, N. Nishiyama, and S. Arai, "Continuous Wave Operation of Thin Film Lateral Current Injection Lasers Grown on Semi-Insulating InP Substrate," *Japanese Journal of Applied Physics,* vol. 49, p. 040205, 2010.

[24] T. Okumura, M. Kurokawa, D. Kondo, H. Ito, N. Nishiyama, and S. Arai, "Lateral Current Injection Type GaInAsP/InP DFB Lasers on SI-InP Substrate," *2009 Ieee 21st International Conference on Indium Phosphide & Related Materials (Iprm),* pp. 178-181, 2009.

[25] P. Kozodoy, H. Xing, S. P. DenBaars, U. K. Mishra, A. Saxler, R. Perrin, S. Elhamri, and W. C. Mitchel, "Heavy doping effects in Mg-doped GaN," *Journal of Applied Physics,* vol. 87, p. 1832, 2000.

[26] K. Kumakura, T. Makimoto, and N. Kobayashi, "Mg-acceptor activation mechanism and transport characteristics in p-type InGaN grown by metalorganic vapor phase epitaxy,"

Journal of Applied Physics, vol. 93, p. 3370, 2003.
[27] T. Katsuno, Y. Liu, D. Li, H. Miyake, K. Hiramatsu, T. Shibata, and M. Tanaka, "n-type conductivity control of AlGaN with high Al mole fraction," *physica status solidi (c),* vol. 3, pp. 1435-1438, 2006.
[28] J. Verma, J. Simon, V. Protasenko, T. Kosel, H. Grace Xing, and D. Jena, "N-polar III-nitride quantum well light-emitting diodes with polarization-induced doping," *Applied Physics Letters,* vol. 99, p. 171104, 2011.
[29] J. Simon, V. Protasenko, C. Lian, H. Xing, and D. Jena, "Polarization-Induced Hole Doping in Wide-Band-Gap Uniaxial Semiconductor Heterostructures," *Science,* vol. 327, pp. 60-64, 2009.
[30] L. Zhang, K. Ding, N. X. Liu, T. B. Wei, X. L. Ji, P. Ma, J. C. Yan, J. X. Wang, Y. P. Zeng, and J. M. Li, "Theoretical study of polarization-doped GaN-based light-emitting diodes," *Applied Physics Letters,* vol. 98, p. 101110, 2011.
[31] L. Zhang, K. Ding, J. C. Yan, J. X. Wang, Y. P. Zeng, T. B. Wei, Y. Y. Li, B. J. Sun, R. F. Duan, and J. M. Li, "Three-dimensional hole gas induced by polarization in (0001)-oriented metal-face III-nitride structure," *Applied Physics Letters,* vol. 97, p. 062103, 2010.
[32] K. Dong, D. Chen, B. Liu, H. Lu, P. Chen, R. Zhang, and Y. Zheng, "Characteristics of polarization-doped N-face III-nitride light-emitting diodes," *Applied Physics Letters,* vol. 100, p. 073507, 2012.
[33] S. Li, M. E. Ware, V. P. Kunets, M. Hawkridge, P. Minor, J. Wu, and G. J. Salamo, "Polarization induced doping in graded AlGaN films," *physica status solidi (c),* vol. 8, pp. 2182-2184, 2011.
[34] Y. Yan Zhang and Y. An Yin, "Performance enhancement of blue light-emitting diodes with a special designed AlGaN/GaN superlattice electron-blocking layer," *Applied Physics Letters,* vol. 99, p. 221103, 2011.
[35] Y.-Y. Zhang, X.-L. Zhu, Y.-A. Yin, and J. Ma, "Performance Enhancement of Near-UV Light-Emitting Diodes With an InAlN/GaN Superlattice Electron-Blocking Layer," *Ieee Electron Device Letters,* vol. 33, pp. 994-996, 2012.
[36] S. Choi, M. H. Ji, J. Kim, H. J. Kim, M. M. Satter, P. D. Yoder, J. H. Ryou, R. D. Dupuis, A. M. Fischer, and F. A. Ponce, "Efficiency droop due to electron spill-over and limited hole injection in III-nitride visible light-emitting diodes employing lattice-matched InAlN electron blocking layers," *Applied Physics Letters,* vol. 101, Oct 15 2012.
[37] Y.-K. Kuo, Y.-H. Chen, J.-Y. Chang, and M.-C. Tsai, "Numerical analysis on the effects of bandgap energy and polarization of electron blocking layer in near-ultraviolet light-emitting diodes," *Applied Physics Letters,* vol. 100, p. 043513, 2012.

TASK 4: III-N UV Laser Processing, Testing, and Characterization

In the past few months, we conducted focused work on the DUV laser processing and characterization development. We have developed a robust HfO_2/SiO_2 dielectric mirror coating processes for < 250 nm DUV laser bars in this program and this processing step enables the realization of high-reflectivity (HR) end-mirrors on cleaved facets for DUV optically pumped lasers. The fabricated laser bars with the HR facet coatings shows a reduced threshold pumping power density from 250 (cleaved facets without HR end-mirror coating) to 180 kW/cm^2 (with HR end-mirror coatings on both ends.) The laser bar shows an emission wavelength (λ) of 249

nm and a preferential TE polarization. The internal loss of 2 cm^{-1} and the threshold modal gain of 10.9 cm^{-1} are also estimated from the experiments. These results indicate that the facet-coating using the HfO_2/SiO_2 dielectric mirror effectively improve the lasing characteristics of DUV lasers.

1. Fabrication processing development and characterizations of optically pumped sub-250-nm DUV laser with HfO_2/SiO_2 end-mirror coatings:

Since the waveguide structure of the optically pumped laser does not require an additional mesa for the index guiding in the lateral dimension, the optically-pumped laser fabrication processing step starts with a backside wafer thinning step that was previously developed in this program. The lapping processing developed at Georgia Tech features a unique high lapping rate chemical-mechanical lapping & polishing process using a commercially available polishing fluid (SF1, Logitech). For AlN substrates, the lapping rate can be as high as 100 μm per hour and the lapped surface has a roughness of less than 1 nm using this process, which greatly enhances the processing throughput of the AlN wafer thinning process. The lapped and polished DUV laser diode samples have a nominal thickness of 75 to 100 microns for the subsequent laser bar cleaving step. High-quality end-mirror of the DUV laser bar can be achieved by cleaving the devices along the m-plane. The detailed processing developments were reported in previous quarterly reports and will not be repeated herein. One of the major efforts during this report period is to integrate the previously developed HR facet coating process into the optically pumped laser bar process. The successful this processing integration effort leads to a further improvement of the optically pumped laser performance in the pump threshold power reduction. These development progresses will be discussed as follows.

(i) High-reflectivity facet coating on DUV laser bars:

Due to the large contrast of the refractive indices between HfO_2 ($n \sim 2.2$ and $k \sim 3\times10^{-3}$ cm^{-1} at $\lambda = 250$ nm) and SiO_2 ($n \sim 1.4$ and $k \sim 2.5\times10^{-3}$ cm^{-1} at $\lambda = 250$ nm)[5], distributed Bragg reflectors (DBRs) with high reflectivity ($R > 92\%$) and wide stop band can be achieved with a small number of HfO_2/SiO_2 pairs (< 6 pairs), which greatly promote the feasibility of high-quality end-facet mirror fabrication for DUV lasers. A customized facet coating jig capable of mounting multiple laser bars for single loading processing was used in this processing module and the deposition of dielectric layers is performed in a high-vacuum evaporator system (CHA Mark-40.) The deposition conditions for repeatable 6-pair quarter-wave-plate SiO_2/HfO_2 DBR was developed in this program. For each pair of HfO2/SiO2 quarter-wave-plate, the thickness of HfO_2 is 28 nm and SiO_2 is 45 nm, respectively. The intended center wavelength of the stop-band is 250 nm. Figure 2 (a) shows the reflectivity spectrum of a 6-pairs SiO_2/HfO_2 DBR fabricated on a glass substrate as a companion sample in the LD processing. The measurement was carried out under the normal incidence condition. For three individual deposition runs spanning across a period of a few months, it is shown that a reflectivity (R) of greater than 96% and a stop band of greater than 60 nm was consistently achieved in the fabrication runs, as shown in Figure 2 (b). The averaged reflectivity is 96.5 % with the standard deviation of 0.2 % and the averaged center wavelength of the spectra is 255.8 nm with the standard deviation of 0.76 nm. The spectral variation of center wavelength is < 5 nm across a 2×2 cm^2 square area on the companion samples. Although the slight discrepancy between the designed center wavelength and the experimental data, with a wide stop band of > 60 nm, the slight shifting of the center wavelengths did not adversely affect the objective of providing HR coating on LD mirror facets

for emission wavelength around 250 nm.

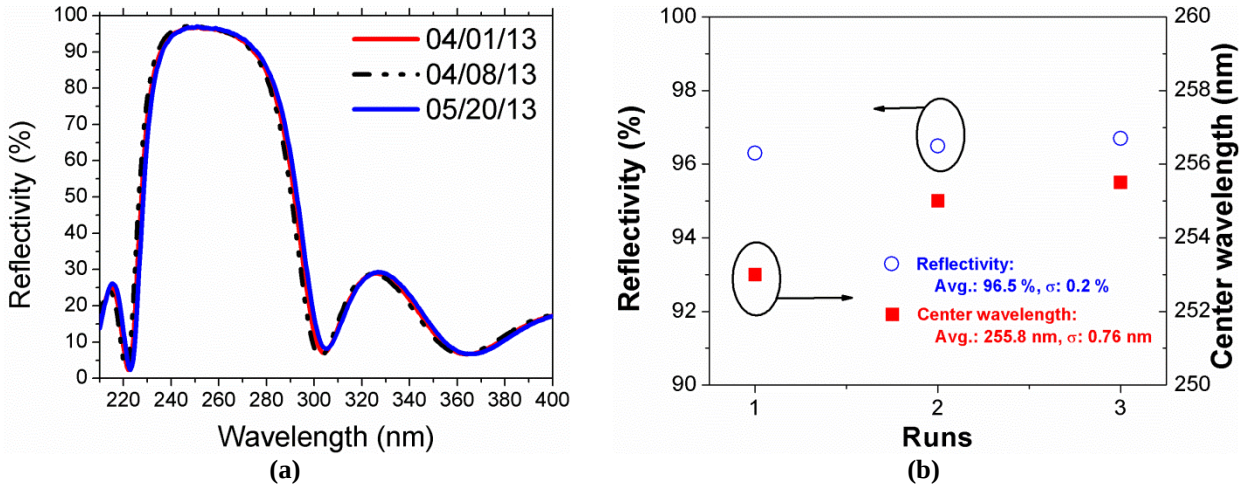

Figure 14. (a) The measured reflectance curves of HfO_2/SiO_2 DBR films designed at a center wavelength of 255 nm; (b) A summary plot showing the averaged reflectivity and the center wavelength of the stop band of the 6-pair HfO_2/SiO_2 DBR for each trial run.

(ii) Optically pumped DUV laser characterizations:
(iii)

Optical pumping system description:

We have completed the optical pumping system setup for the DUV laser measurement at Georgia Tech. The system setup was described in detailed in earlier reports and has been functional since July 2012. As a summary, system schematic system setup is show in Figure 15(a). Standard operation procedures have also been setup for quick turn-around DUV laser evaluation. The excitation source is ArF Excimer laser (λ= 193 nm) with a pulse width of 20 ns at a repetition rate of 10 Hz and the output power ranges from 10 mJ to 200 mJ. Shown in Figure 15 (b) is the beam controlling path setup of the measurement system. In the DUV LD measurement, the laser beam was shaped into a 0.1×1.27 cm^2 rectangular emission area using a customized optical aperture (identified as a "slit" in **Figure 15**(a)). A 45-degree DUV-grade mirror was inserted in the light path after the slit to redirects the beam for pump power density calibration when necessary during the measurements.

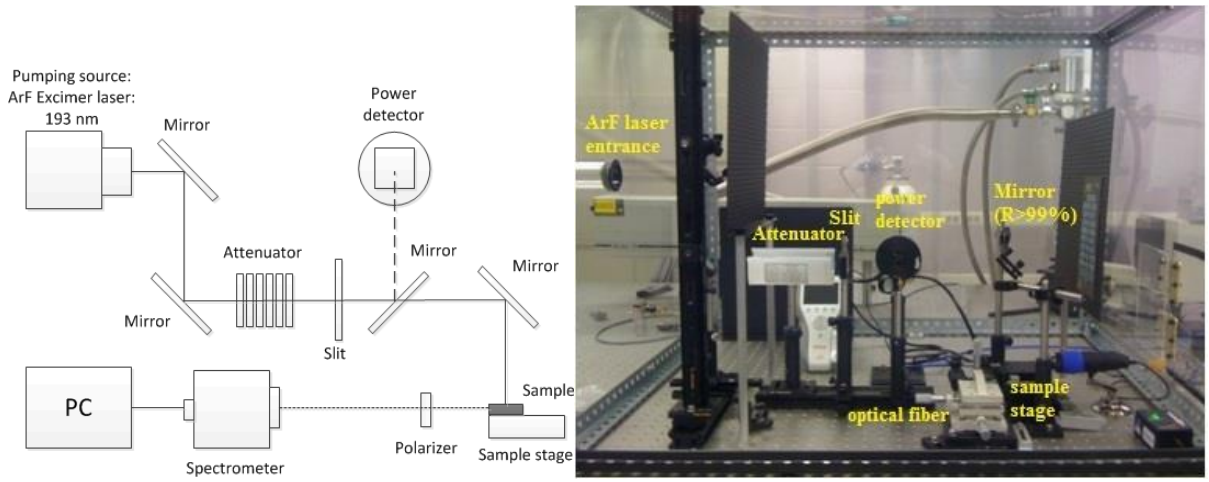

(a) (b)

Figure 15. (a) A schematic of an optically pumped laser measurement system at Georgia Tech and (b) a picture showing the corresponding optical system setup.

The sapphire substrates serve as digital attenuators that can be inserted before optical aperture to further reduce the pump power density when necessary. A Glan-Laser α-BBO polarizer was used for selecting the polarization of the photon emission from the DUV laser bars. The light emission of the optically pumped laser bars are measured from the cleaved *m*-plane facets of the fabricated laser bars by coupling the photon emissions into an UV optical fiber. An Ocean Optics Maya-2000 Pro spectrometer with a spectral resolution of 0.2 nm was used for the emission spectrum measurements.

Characteristics of optically pumped DUV laser bars

In this experiment, both sides of the DUV laser bars were coated with HR HfO_2/SiO_2 mirrors. As shown in **Figure 16** (a), the emission spectra of a DUV laser bar with double-sided dielectric mirror coatings shows a stimulated emission at λ= 249 nm for an optical pumping power of > 160 kW/cm^2. At a pumping power of 265 kW/cm^2, the spectral linewidth of 0.6 nm is also achieved. The narrow emission spectral linewidth is partly attributed to the formation of high-quality facet mirrors and the HR coatings. Also shown in **Figure 16** (a) are the reflectivity spectra of the front-side and the backside facet mirrors measured on a companion samples along with each facet coating runs. The reflectivity spectrum were measured by an ultraviolet-visible spectrometer (Shimadzu UV2401PC). HR mirrors with R = 92 % and 97 % at λ = 249 nm were achieved on the front- and rear-side facets, respectively.

We also observed a preferential TE-polarization in the emission spectrum of the 249-nm DUV laser bars, as shown in Figure 16 (b). The degree of polarization (*P*), defined as $P = (I_{TE} - I_{TM})/(I_{TE} + I_{TM})$, shows a ~100% TE polarization in the laser bars. The TE-dominant emission is attributed to the in-plane compressive strain in the quantum-confined structure[6]. In our study, we also monitor the optical output characteristics throughout the facet coating process. Figure 17 shows a summary of the measured optical output power versus the excitation power density (*L-L* curve) for the fabricated DUV laser bar before the facet coating, with rear-side 6-pair HR coating only, and with both facet coatings, respectively. It is shown that the threshold pumping power density (P_{th}) was reduced from 250 to 215 kW/cm^2 after a dielectric reflector (R = 97%) was applied on the rear-side of the facet. Another reduction in P_{th} from 215 to 180 kW/cm^2 was

achieved after the front-side HR coating (R = 92%) was fabricated. Overall, P_{th} was reduced by ~ 28% with the HR coatings in the fabricated DUV laser. In addition, we also observed significant drop in the slope efficiency after both facet coatings. The result suggests that these HR DBRs are effectively reducing the round-trip loss and a high-Q resonant cavity was achieved in the laser bars.

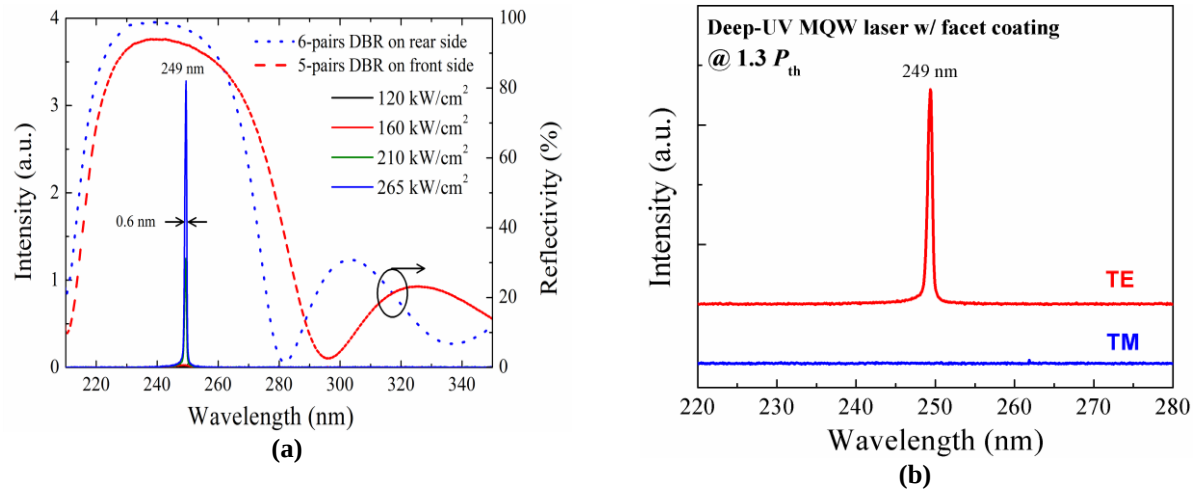

Figure 16 (a) A room-temperature emission spectra of a AlGaN-based MQW laser with HfO_2/SiO_2 dielectric mirrors coated on both facets and the corresponding reflectivity spectra of the front-side (6-pairs) and rear side (5-pairs) DBR mirrors and (b) The TE and TM-mode emission spectra of the same laser bar operating above the pump threshold at room temperature. An offset was applied on the TE emission spectrum for visual clarity.

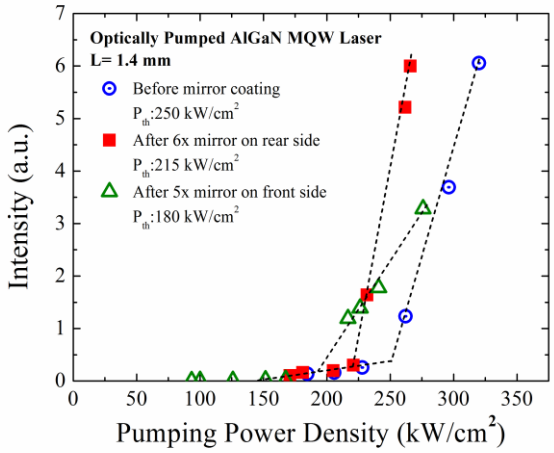

Figure 17. A summary plot of the light-output intensity versus the optical pump power density (the L-L curves) for an AlGaN-based MQW DUV laser with cleaved facets only (hollow circle in blue), after the rear-side mirror coating (solid square in red), and after the double-sided facet coating (hollow triangle in green).

The internal loss and the threshold gain of the AlGaN-based MQW laser can also be estimated from the L-L curves. Assuming that the modal reflectance is close to the externally measured value, the internal loss (α_i) can be determined by[7]:

$$\alpha_i = \frac{1}{L} \times \frac{\eta_d' - \eta_d}{\left(\frac{\eta_d}{\ln\frac{1}{\sqrt{R_1 R_2}}} - \frac{\eta_d'}{\ln\frac{1}{\sqrt{R_1' R_2'}}}\right)} \quad (1)$$

, where L (= 1.4 mm) is the cavity length; R_1 and R_2 (= R_1 =18%) are the reflectivity of the as-cleaved facets; R_1' (= 92 %) and R'_2 (= 97 %) are the reflectivity of the front-side and the rear-side coated facets, respectively and η'_d and η_d are the differential quantum efficiency after the facet coating and the differential quantum efficiency of the as-cleaved laser bar, respectively. Although the output light intensity is in the arbitrary units, one may assume that the measured light output is linearly proportional to the actual output power of the laser. As a result, η_d can be found by:

$$\eta_d \propto \frac{1}{F}\frac{dP_{out}}{dP_{in}} \propto \frac{1}{F}\frac{dI_{out}}{dP_{in}} \quad (2)$$

, where P_{in} and P_{out} represent the input and output power, respectively, and I_{out} is the light output intensity. The fraction of the output power (F) measured from the front-side of the facet with respect to the total optical output power can therefore be assessed by:

$$F = \frac{1-R_1}{(1-R_1+\sqrt{R_1/R_2}\,(1-R_2)} \quad (3)$$

In this case, F is 0.5 and 0.73 for the laser bar before and after facet coatings, respectively. Since the proportionality factor in Eq. (2) has no effect on Eq. (1), α_i of 2 cm^{-1} can be found from this calculation. Thus, the threshold modal gain (g_{th}) can also be calculated with

$$\Gamma g_{th} = \alpha_i + \frac{1}{L}\ln\left(\frac{1}{\sqrt{R_1 R_2}}\right) \quad (4)$$

g_{th} is reduced from 63 cm^{-1} for the as-cleaved laser bar to 10.9 cm^{-1} for the same laser bar coated with HR mirrors on both sides. It should be noted that g_{th} is approximately an order of magnitude lower than that for other AlGaN-based MQWs grown on 6H-SiC substrate with emission wavelengths in the $\lambda \sim 250$ nm ranges[8].

A summary of state-of-the-art performance for optically-pumped DUV lasers is shown in Table **2**. It is clear that the Georgia Tech team successfully demonstrated DUV optically-pumped lasers ($\lambda < 250$ nm) with comparable threshold optically pumping power density with PARC's reported laser performance at similar emission wavelengths. Using the HR dielectric mirror coatings, we have also achieved the lowest-threshold optically pumped DUV laser at $\lambda <$ 250 nm reported to date. The results suggest high-quality epitaxial growth has been achieved in GT's MOCVD system.

Table 2: state-of-the-art performance characteristics comparison of optically-pumped DUV lasers

Affiliation	**Laser structure summary (MQWs; WG; cladding layer; substrate)**	**Excitation wavelength (nm)**	**Cavity length (mm)**	**Lasing wavelength (nm)**	**P_{th} (kW/cm^2)**	***Ref.* (year)**
Kohgakuin University	$Al_{0.66}GaN/Al_{0.76}GaN$ MQWs; $Al_{0.76}GaN$;$A_{l0.84}GaN$;4H-SiC	193	0.45	241.5	1200	2004 [9]
Ioffe Institute, Russia	$Al_{0.39}GaN/Al_{0.49}GaN$ MQW; $Al_{0.49}GaN$; $A_{l0.66}GaN$;Sapphire	266	1	303	800	2004 [10]
PARC	$Al_xGa_{1-x}N/Al_yGa_{1-y}N$ MQWs; $Al_{0.7}Ga_{0.3}N$; AlGaN; AlN	248	1	267	126	2011 [11]
GT	AlN (cap); $Al_{0.60}GaN/Al_{0.75}GaN$ MQWs; AlGaN; AlN	193	1.23	243.5	427	2012 [12]
GT	AlN (cap); $Al_{0.60}GaN/Al_{0.75}GaN$ MQWs; AlGaN; AlN	193	1.25	246.8	455	2012
GT	AlN (cap); $Al_{0.60}GaN/Al_{0.75}GaN$ MQWs; AlGaN; AlN	193	1.45	243.5	297	2013
GT	AlN (cap); $Al_{0.60}GaN/Al_{0.75}GaN$ MQWs; AlGaN; AlN	193	1.4	249	180*	2013

*employing HfO_2/SiO_2 mirror coatings

Fabrication processing development for deep-UV LEDs/ LDs

(i) Processing module development for baseline edge-emitting device processing:

We also fabricated gain-guided laser diode in this period. Shown in **Figure 18**(a) is a schematic cross-sectional view of a laser diode heterostructure. The device fabrication starts with a ridge waveguide etching using an inductively coupled plasma (ICP) etching tool. A photo-enhanced surface treatment is conducted to remove post-dry-etching-induced surface damage. Vanadium-based metal ohmic contact stack was deposited to form the ohmic contact to *n*-type AlGaN (Al > 50%) next to the mesa stripes on the front-side of the wafer. Shown in **Figure 18**(b) is an SEM picture of a fabricated AlGaN waveguide that shows a two-mesa device structure before the p-type metal was deposited. Ni/Ag-based metal stack was then evaporated on the ridged mesa for the *p*-type contact. After the ohmic contact annealing, an additional metal layer (Ti/Au) were deposited to achieve a lower resistance in the p-metal region. The devices were passivated in using a spin-on-glass with low curing temperature, followed by a via-hole opening process. A 1-μm thick interconnect layer was deposited to complete the front-side device processing. The back-side processing involves an AlN substrate thinning and a laser bar cleaving processes, which are described in the optically-pumped laser bar fabrication sections. **Figure 19** (a) and (b) show photographs of UV laser diodes fabricated on a 1.5-cm-diameter wafer of a bulk AlN substrate before and after facet cleaving, respectively.

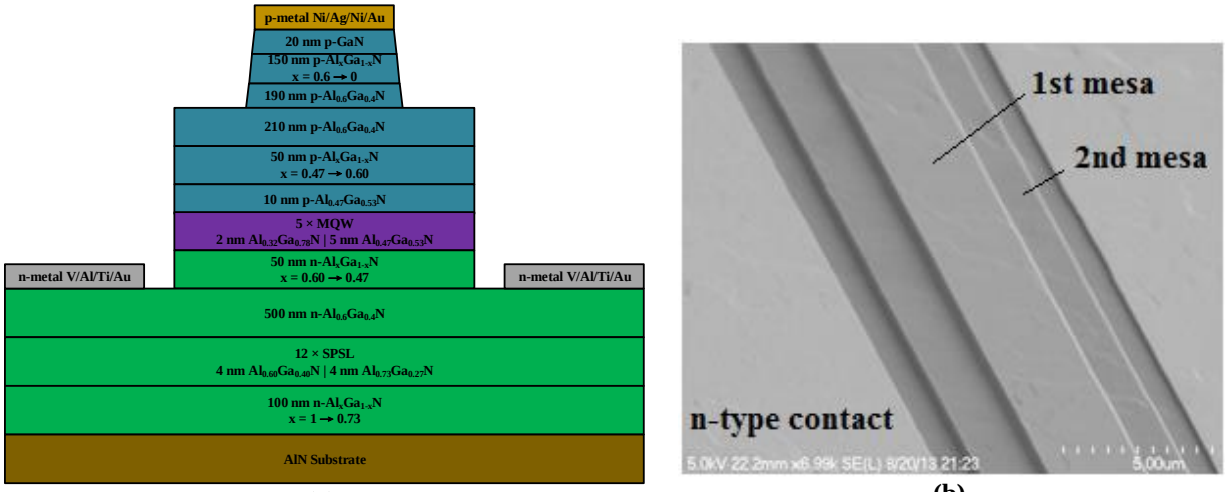

(a) **(b)**

Figure 18 (a) Schematic diagram of the inverse tapered laser diode structure on AlN template. (b) SEM image of the ridge waveguide after n-type metal evaporation.

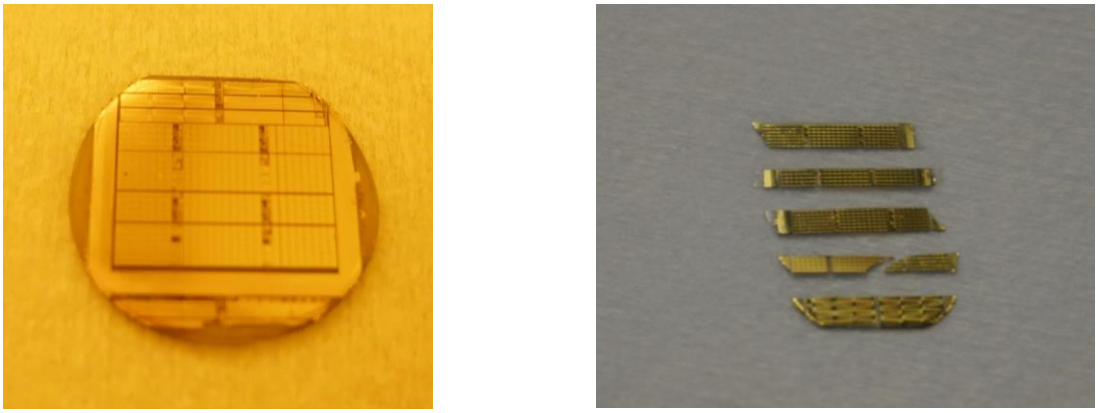

(a) **(b)**

Figure 19 (a) and (b) show the photographs of fully processed UV laser diodes fabricated on a 1.5-cm-diameter wafer of bulk AlN before and after facet cleaving, respectively. The wafer contains several hundred gain-guided laser diodes for testing.

(ii) I-V Characteristics of fabricated waveguide structure:

Figure 20 (a) shows a d.c. I-V characteristics for a fabricated device. This device has a ridge width of 3.5 µm and cavity length of 1.5 mm. A current level of 225mA was measured that is equivalent to a current density of 10 kA/cm^2. The device has a turn-on voltage of ~8 V and a serial resistance of 15 Ω.

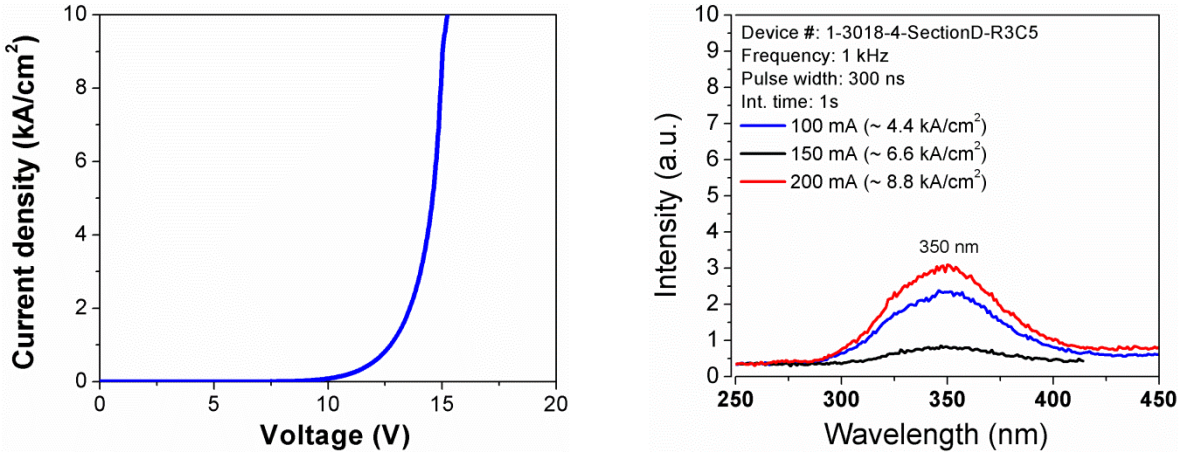

Figure 20 (a) and (b) show the photographs of fully processed UV laser diodes fabricated on a 1.5-cm-diameter wafer of bulk AlN before and after facet cleaving, respectively. The wafer contains several hundred gain-guided laser diodes for testing.

(ii) EL Characteristics of fabricated waveguide structure:

The LD was driven under the pulsed current mode with a pulse width of 300 ns and a repetition frequency of 1 kHz. **Figure 20**(b) shows the room-temperature spontaneous emission spectrum of a stripe laser heterostructure operating under the pulse conditions. The devices showed very wide emission spectra with a peak wavelength of 350 nm and a FWHM of > 60 nm. The reasons of the deviation from the structure design that showed long wavelength emission characteristics are still under investigation.

4. PUBLICATIONS: List of Publications Authored in this Program

1. H. J. Kim, S. Choi, D. Yoo, J.-H. Ryou, R. D. Dupuis, M. Hawkridge, and Z. Liliental-Weber, "Digitally-alloyed modulated precursor flow epitaxy of ternary AlGaN with AlN and GaN binary sub-layers and observation of compositional inhomogeneity," *J. Electron. Mater.*, Vol. 39, No. 5, pp. 466–472 (2010)
2. M. Abid, , T. Moudakir, S. Gautier, G. Orsal, A. E. Naciri, Z. Djebbour, J.-H. Ryou, G. Patriarche, H.-J. Kim, Z. Lochner, K. Pantzas, K. D. Alamarguy, F. Jomard, R. D. Dupuis, and A. Ougazzaden, "New generation of Distributed Bragg Reflectors based on BAIN/AIN structures for deep UV-optoelectronic applications", CLEO:2011 Laser Science to Photonic Applications, 2 (2011).
3. Md. M. Satter, H. J. Kim, Z. Lochner, J.-H. Ryou, S.-C. Shen, R. D. Dupuis, and P. D. Yoder, "Design and analysis of 250nm AlInN laser diodes on AlN substrates using tapered electron blocking layers," IEEE J. Quantum Electron. 48 (5), 703–711 (2012).
4. M. Abid, T. Moudakir, G. Orsal, S. Gautier, A. En Naciri, Z. Djebbour, J.-H. Ryou, G. Patriarche, L. Largeaud, H. J. Kim, Z. Lochner, K. Pantzas, D. Alamarguy, F. Jomard, R. D. Dupuis, J.-P. Salvestrini, P. L. Voss, and A. Ougazzaden, "Distributed Bragg reflectors based on diluted boron-based BAlN alloys for deep ultraviolet optoelectronic applications," Appl. Phys. Lett. 100 (5), 051101-1–4 (2012).
5. Md. M. Satter, Z. Lochner, J.-H. Ryou, S.-C. Shen, R. D. Dupuis, and P. D. Yoder, "Polarization matching in AlGaN-based multiple quantum well deep ultraviolet laser diodes on AlN substrates using quaternary AlInGaN barriers," J. Lightwave Technol. 30(18), 3017-25 (2012).
6. Md. M. Satter, H. J. Kim, Z. Lochner, J.-H. Ryou, S.-C. Shen, R. D. Dupuis, and P. D. Yoder, "Design and analysis of 250nm AlInN laser diodes on AlN substrates using tapered electron blocking layers," IEEE J. Quantum Electron. 48 (5), 703–711 (2012).
7. Z. Lochner, X.-H. Li, T.-T. Kao, M. M. Satter, H. J. Kim, S.-C. Shen, P. D. Yoder, J.-H. Ryou, R. D. Dupuis, K. W. Sun, Y. O. Wei, T. Li, A. M. Fischer, and F. A. Ponce. "Stimulated emission at 257 nm from an optically-pumped AlGaN/AlN heterostructure on AlN substrate," Physica Status Solidi A, Vol. 210, pp. 1768-1770, 9 September 2013.
8. Z. Lochner, T-T. Kao, Y.-S. Liu, X-H. Li, Md. M. Satter, S.-C. Shen, P. D. Yoder, J.-H. Ryou, R. D. Dupuis, Y. Wei, H. Xie, A. Fischer, and F.A. Ponce, "Deep-Ultraviolet Lasing at 243 nm from Photo-Pumped AlGaN/AlN Heterostructure on AlN Substrate," Appl. Phys. Lett., Vol. 102, p. 101110 (2013).
9. Z. Lochner, T-T. Kao, Y.-S. Liu, X. Li, M. Satter, S-C. Shen, P. D. Yoder, J-H. Ryou, R. D. Dupuis, Y. Wei, H. Xie, A. Fischer, and F.A. Ponce, "Room-temperature optically pumped AlGaN-AlN multiple-quantum-well lasers operating at λ<260 nm grown by metalorganic chemical vapor deposition," Proc. of SPIE Vol. 8625, 862519 (2013).
10. M. M. Satter, Z. Lochner, J. H. Ryou, S. C. Shen, R. D. Dupuis, and P. D. Yoder, "AlGaN-Based Lateral Current Injection Laser Diodes Using Regrown Ohmic Contacts," *IEEE*

Photonics Technology Letters, Vol. 25, pp. 313-316 (2013).

5. CONFERENCE PRESENTATIONS: List of Presentations in this Program

1. Zachary Lochner, , Tsung-Ting Kao, Yuh-Shiuan Liu**,** Xiaohang Li, Md. Mahbub Satter, Shyh-Chiang Shen, Douglas Yoder, Jae-Hyun Ryou, Yong Wei, Hongen Xie, Alec M. Fischer, Fernando A. Ponce, and Russell D. Dupuis' "Room-temperature optically pumped AlGaN-AlN multiple-quantum-well lasers operating at <260nm grown by metalorganic chemical vapor deposition," *SPIE OPTO Symposium, Photonics West 2013*, San Francisco, CA, USA, Feb. 2013.
2. Z. Lochner, Y-S. Liu, T-T. Kao, X. Li, M. Satter, J-H. Ryou, S-C. Shen, P. D. Yoder, R. D. Dupuis, Y. Wei, H. Xie, A. Fischer, F. Ponce, "Optically pumped AlGaN quantum-well lasers at ~243.5 nm grown by MOCVD on AlN substrates", submitted to European Materials Research Society (EMRS 2013), France, May 2013.
3. Zachary Lochner, Yuh-Shiuan Liu, Tsung-Ting Kao, Xiaohang Li, Md. Mahbub Satter, Jae-Hyun Ryou, Shyh-Chiang Shen, P. Douglas Yoder, Russell D. Dupuis, "Stimulated emission at 243.5 nm from optically pumped quantum-well heterostructures grown by MOCVD on AlN substrates," Submitted to 2013 Electronic Materials Conference, June 2013.
4. Xiao-Hang Li, Zachary Lochner, Yuh-Shiuan Liu, Tsung-Ting Kao, Md. Mahbub Satter, Jae-Hyun Ryou, Shyh-Chiang Shen, P. Douglas Yoder, and Russell D. Dupuis, "Growth of High Al-Content AlGaN on AlN/ Sapphire Templates by High-Temperature Metalorganic-Chemical-Vapor Deposition," Submitted to 2013 Electronic Materials Conference, June 2013.
5. Z. Lochner, Y.-S. Liu, T.-T. Kao, X. Li, M. Satter, J.-H. Ryou, S.-C. Shen, P. D. Yoder, R. D. Dupuis, Y. Wei, H. Xie, A. Fischer, F. Ponce, "Optically pumped AlGaN quantum-well lasers at ~243.5 nm grown by MOCVD on AlN substrates", *European Materials Research Society (EMRS 2013)*, Strasbourg, France, May 2013.
6. Z. Lochner, Y.-S. Liu, T. T. Kao, X. Li, M. Satter, J.-H. Ryou, S.-S. Shen, P.D. Yoder, R.D. Dupuis, "Stimulated emission at 243.5 nm from optically pumped quantum-well heterostructures grown by MOCVD on AlN substrates," *55th Electronic Materials Conference Notre Dame*, Southbend, IN., June 2013
7. X. Li, Z. Lochner, Y.-S. Liu, T.-T. Kao, M. Satter, J.-H. Ryou, S.-S. Shen, P. D. Yoder, R. D. Dupuis, "Growth of High Al-Content AlGaN on AlN/ Sapphire Templates by High-Temperature Metalorganic-Chemical-Vapor Deposition," *55th Electronic Materials Conference Notre Dame*, Southbend, IN., June 2013.
8. Y.-S. Liu, T.-T. Kao, Z. Lochner, X. Li, M. Satter, J.-H. Ryou, S.-S. Shen, P. D. Yoder, T. Detchprohm, R. D. Dupuis, "Optically pumped AlGaN based Deep-ultraviolet multi-quantum-well laser grown by metalorganic chemical vapour deposition," *ICNS-10*, Washington, DC, August 2013

9. M. Satter, V. Kolesov, T. Philip, Y.-S. Liu, T.-T. Kao, Z. Lochner, X. Li, J.-H. Ryou, S.-S. Shen, T. Detchprohm, R. D. Dupuis, P. D. Yoder, "Theoretical Analysis of Strategies for Improving P-Type Conductivity in Wurtzite III-Nitride Devices for High-Power Opto- and Microelectronic Applications," *ICNS-10,* Washington, DC, August 2013.
10. X. Li, Z. Lochner, Y.-S. Liu, T.-T. Kao, M. Satter, J.-H. Ryou, S.-S. Shen, P. D. Yoder, T. Detchprohm, R. D. Dupuis, "Stimulated Emission at 256.1 nm with a Low Threshold Optical Pumping Power density from AlGaN Multiple Quantum Well grown at High Temperature on Sapphire," *ICNS-10,* Washington, DC, August 2013.

References

[1] Katsuno, T., Liu, Y., Li, D., Miyake, H., Hiramatsu, K., Shibata, T. and Tanaka, M., "n-type conductivity control of AlGaN with high Al mole fraction," *Phys. Status Solidi C*, **3**, 1435–1438. (2006).

[2] M. L. Nakarmi, K. H. Kim, K. Zhu, J. Y. Lin, and H. X. Jiang, "Transport properties of highly conductive *n*-type Al-rich $Al_xGa_{1-x}N$ ($x >= 0.7$),"*Appl. Phys. Lett.* **85**, 3769 (2004).

[3] J. Mickevicius, J. Jurkevicˇius, K. Kazlauskas, A. Zukauskas, G. Tamulaitis, M. S. Shur, M. Shatalov, J. Yang, and R. Gaska: Appl. Phys. Lett. 100, 081902 (2012).

[4] T. Wunderer, C. Chua, Z. Yang, J. Northrup, N. Johnson, G. Garrett, H. Shen, and M. Wraback: Appl. Phys. Express 4 (2011) 092101.

[5] P. Torchio, A. Gatto, M. Alvisi, G. Albrand, N. Kaiser, and C. Amra, Appl. Opt. **41**, 3256 (2002).

[6] R. G. Banal, M. Funato, and Y. Kawakami, Phys. Rev. B **79**, 121308 (2009).

[7] L. A. Coldren and S. W. Corzine, *Diode lasers and photonic integrated circuits*, 1st ed. (Wiley, New York, 1995).

[8] E. F. Pecora, W. Zhang, A. Y. Nikiforov, J. Yin, R. Paiella, L. D. Negro, and T. D. Moustakas, J. Appl. Phys. **113**, 013106 (2013).

[9] T. Takano, Y. Narita, A. Horiuchi, and H. Kawanishi, Appl. Phys. Lett. 84, 3567 (2004).

[10] V. N. Jmerik, A. M. Mizerov, A. A. Sitnikova, P. S. Kop'ev,1 S. V. Ivanov, E. V. Lutsenko, N. P. ; Tarasuk, N. V. Rzheutskii, and G. P. Yablonskii, Appl. Phys. Lett. 96, 141112 (2010).

[11] T. Wunderer, C. L. Chua, Z. Yang, J. E. Northrup, N. M. Johnson, G. A. Garrett, H. Shen, and M. Wraback, Appl. Phys. Express **4**, 092101 (2011).

[12] Z. Lochner, T. T. Kao, Y. S. Liu, X. H. Li, Md. M. Satter, S. C. Shen, P. D. Yoder, J. H. Ryou, R. D. Dupuis, Y. W, H. Xie, A. Fischer, and F. A. Ponce, Appl. Phys. Lett. **102**, 101110 (2013).